# A mixed space-time and wavenumber-frequency domain procedure for modelling ground vibration from surface railway tracks

S.G. Koroma[1*], D.J. Thompson[1], M.F.M. Hussein[2], E. Ntotsios[1]

[1]*Institute of Sound and Vibration Research, University of Southampton, Southampton, SO17 1BJ, UK*

[2]*Department of Civil and Architectural Engineering, College of Engineering, Qatar University, P.O. Box 2713, Doha, Qatar*

**Abstract**

This paper presents a methodology for studying ground vibration in which the railway track is modelled in the space-time domain using the finite element method (FEM) and, for faster computation, discretisation of the ground using either FEM or the boundary element method (BEM) is avoided by modelling it in the wavenumber-frequency domain. The railway track is coupled to the ground through a series of rectangular strips located at the surface of the ground; their vertical interaction is described by a frequency-dependent dynamic stiffness matrix whose elements are represented by discrete lumped parameter models. The effectiveness of this approach is assessed firstly through frequency domain analysis using as excitation a stationary harmonic load applied on the rail. The interaction forces at the ballast/ground interface are calculated using the FE track model in the space-time domain, transformed to the wavenumber domain, and used as input to the ground model for calculating vibration in the free field. Additionally, time domain simulations are also performed with the inclusion of nonlinear track parameters. Results are presented for the coupled track/ground model in terms of time histories and frequency spectra for the track vibration, interaction forces and free-field ground vibration. For the linear track model, the results from the mixed formulation are in excellent agreement with those from a semi-analytical model formulated in the wavenumber-frequency domain, particularly in the vicinity of the loading point. The accuracy of the mixed formulation away from the excitation point depends strongly on the inclusion of

*Corresponding author, *Email address:* sgkoroma@gmail.com

*Email addresses:* djt@isvr.soton.ac.uk (D.J. Thompson[1]), mhussein@qu.edu.qa (M.F.M. Hussein[2]), E.Ntotsios@soton.ac.uk (E. Ntotsios[1])

through-ground coupling in the lumped parameter model, which has been found to be necessary for both track dynamics and ground vibration predictions.
*Keywords:* Ground vibration, Lumped parameter model, Finite element method, Space-time domain, Wavenumber-frequency domain

## 1. Introduction

The numerical modelling of ground vibration from surface railways has been the focus of much research over the years. When linear parameters are used for the track and ground, the modelling can be readily done in the frequency-wavenumber domain. Sheng et al. [1] studied ground vibration generated by a stationary harmonic load acting on a railway track using a transformation into the frequency-wavenumber domain. The track was modelled as infinite layered beams that are coupled to a horizontally layered ground. This methodology was applied to the case of a load [2] and a train [3] moving along a railway track. These models are based on the assumption that the track geometry is longitudinally invariant, in addition to the assumption of linearity.

However, when complex irregular geometries are to be modelled, more complex approaches such as Finite Elements (FE) and Boundary Elements (BE) are necessary for this problem. These approaches include the so-called two-and-a-half dimensional (2.5D) approach [4, 5, 6], widely used to discretise the cross-section of track and ground, with the longitudinal dimension modelled in the wavenumber domain. Fully three dimensional FE models or coupled FE-BE models in the time domain [7] are required when nonlinear track or soil components [8] are to be included. The use of FE and BE methods in numerical analyses can be very costly in terms of the computational hardware and the time required for the simulations. This is mainly due to the large number of elements required to discretise the ground, particularly in the 3D case.

An alternative, which is widely used in soil-structure interaction problems, e.g. the vibration of machine foundations on a half-space or layered ground [9], is to represent the ground by approximate lumped parameter models consisting of spring, dashpot, and in some cases mass elements. This approach has been applied to ground vibration from surface trains in [10, 11]. The lumped parameter model was formulated based on Lysmer's analogue fitting which, due to its simplicity, is mostly accurate for modelling the asymptotic values of the dynamic stiffness at low and high

frequencies, without capturing mid frequency fluctuations. Triepaischajonsak and Thompson [12] presented a hybrid modelling approach for predicting ground vibration from trains, whereby the track is modelled in the time domain and the ground in the frequency domain. The transfer mobilities of a layered ground were calculated using the dynamic stiffness method [13] for a harmonic load distributed over a circular area at the surface. The effect of the ground was incorporated into the track model by connecting the sleepers to a series of equivalent spring-dashpot systems, the properties of which were obtained by curve fitting the combined ballast/ground dynamic stiffness that makes use of the ground mobilities. In this study, however, the effect of through-ground coupling was not considered. Another hybrid model was presented by Nielsen et al. [14] for predicting ground vibration due to discrete wheel-rail irregularities. The DIFF model [15], which is based in the time domain, was used to obtain the transient wheel-rail contact force and the TRAFFIC model [16], formulated in the frequency-wavenumber domain, utilised this as input to predict the track and ground vibration. The ground was included in DIFF using discrete spring-dashpot-mass systems tuned to minimise the differences in the track receptance computed using DIFF and TRAFFIC.

Wolf [17, 18] presented a systematic procedure for formulating consistent lumped parameter models with real frequency-independent coefficients to represent an unbounded soil medium. In this method, each dynamic stiffness component in the frequency domain, e.g. the vertical stiffness due to a vertical load, can be represented in discrete form as a rational fraction. This is subsequently decomposed into singular, first- and second-order regular parts, depending on the nature of the roots of the rational fraction. These models can provide a high degree of accuracy when sufficiently high order of approximating polynomials are used. They also have the advantage that they can be incorporated into standard FE/BE routines for soil-structure interaction, allowing nonlinear parameters to be readily included in the structure. Damgaard et al. [19, 20] applied this approach to study the dynamic soil-structure interaction of offshore wind turbines on gravity footings and monopiles.

The main purpose of this paper is to develop a procedure for studying railway track dynamics that makes use of both space-time and wavenumber-frequency techniques. The railway track is

modelled in the space-time domain using the FE method, whilst the ground is modelled in the frequency-wavenumber domain. The railway track and ground are coupled through a series of rectangular strips located at the surface of the ground; their vertical interaction is described by a frequency-dependent dynamic stiffness matrix whose elements are represented by discrete lumped parameter models [17, 18]. The framework for deriving this dynamic stiffness matrix is developed, and an iterative curve-fitting routine is adopted to obtain the parameters required to formulate the lumped parameter models. Through-ground coupling in the track/ground model is included within this framework, and the effect of this on ground vibration is also investigated. The mixed formulation is assessed using both frequency and time domain analyses and for linear and nonlinear track parameters. Subsequently, the interaction forces at the ballast/ground interface are calculated in the space-time domain, transformed to the wavenumber domain, and used as input to the ground model for calculating the vibration in the free field.

The dynamic stiffness matrix is derived in Section 2 while the corresponding discrete lumped parameter models that represent it are systematically formulated in Section 3. Section 4 presents an example application of the lumped parameter model to study the dynamic interaction between three rectangular strips. The FE track model is introduced in Section 5 and the procedure for calculating the ballast/ground interaction force is described in Section 6 together with the wavenumber domain transformation and subsequent use as input for free-field ground vibration calculations. A frequency domain analysis is conducted in Section 7 with results presented as frequency spectra for the track vibration, interaction forces and free-field ground vibration. Finally, to demonstrate the application of a mixed formulation, time domain simulations are performed in Section 8 for both linear and nonlinear track models.

## 2. Wavenumber-frequency domain modelling of the ground

The ground vibration due to a harmonic load distributed over a rectangular strip at the ground surface was studied by Jones et al. [21]. In this section, this formulation will be extended to account for the interaction between multiple rectangular strips.

Figure 1 shows a three dimensional model of a railway track/ground system in which the ground is idealised either as a half-space or as one or more layers overlying a half-space. The

track rests on the surface of the ground with its length along the $x-$direction and its centre line located at $y = 0$. The ground is coupled to the track through the ballast beneath each sleeper, taking

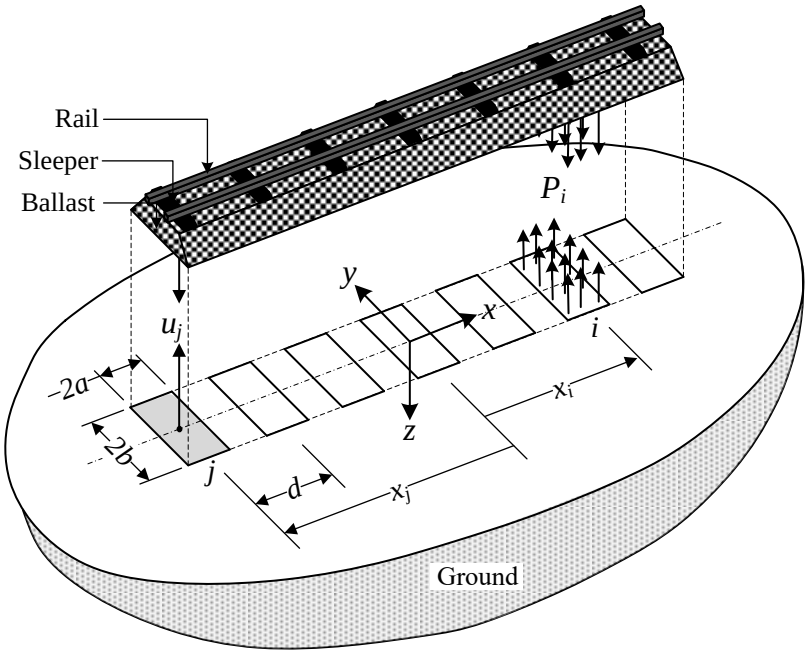


Figure 1: Three dimensional railway track/ground interaction model. The track loads are applied on a series of rectangular strips used for the coupling of the track and ground

into account only the vertical interaction forces. Such an assumption is reasonable for this application, since the vertical dynamics is dominant in railway-induced ground vibration. Furthermore, since the ballast is relatively flexible in comparison with, say, a rigid foundation, lateral dynamics induced by vertical forces can neglected. The vertical interaction forces at the ballast/ground interface are considered to be distributed over a series of $N$ discrete rectangular strips. Each strip has length $2a$ in the $x-$direction and width $2b$ in the $y-$direction. The spacing between the centres of two consecutive strips is $d$ and is equivalent to the spacing of the sleepers in the track.

The formulation is given here for a homogeneous half-space. Since the extension to a layered ground is quite straightforward, the same approach will also be used to investigate the effect of a layer overlying a half-space.

Consider an evenly distributed impulsive load of unit magnitude and of infinitesimal duration

applied at time $t = \tau$ on an arbitrary rectangular strip whose centre is located at $x = x_i, y = 0$. This load can be expressed mathematically as

$$P(x, y, t) = \frac{1}{4ab} \left[\mathcal{H}(x - x_i + a) - \mathcal{H}(x - x_i - a)\right] \left[\mathcal{H}(y + b) - \mathcal{H}(y - b)\right] \delta(t - \tau), \tag{1}$$

where $\mathcal{H}(\cdot)$ is the Heaviside step function and $\delta(\cdot)$ the Dirac delta function. Other load distributions can be assumed such as a trapezoidal function or a 'bell-shaped' function as used by Andersen and Clausen [22] for wind turbine footings.

Since the ground is formulated in the wavenumber-frequency domain, it is expedient to transform Eq. (1) into the same domain. This can be done by performing triple Fourier transformations from the $(x, y, t)$ domain to $(\xi, \gamma, \omega)$ domain as follows

$$\breve{P}(\xi, \gamma, \omega, x_0, \tau) = \frac{\sin \xi a \sin \gamma b}{ab\xi\gamma} \mathrm{e}^{-\mathrm{i}(\xi x_i + \omega\tau)}, \tag{2}$$

where $\omega$ is the angular frequency, and $\xi$ and $\gamma$ are the wavenumbers in the $x$ and $y$ directions respectively.

The ground displacement in the wavenumber-frequency domain due to this impulse is given by

$$\breve{U}_g(\xi, \gamma, \omega, x_0, \tau) = \breve{G}(\xi, \gamma, \omega) \mathrm{e}^{-\mathrm{i}(\xi x_i + \omega\tau)}, \tag{3}$$

where $\breve{G}(\xi, \gamma, \omega)$ is the Green's function of the ground in the wavenumber-frequency domain due to a rectangular strip load with unit magnitude centred at the origin. $\breve{G}(\xi, \gamma, \omega)$ is given by [23]

$$\breve{G}(\xi, \gamma, \omega) = \frac{1}{\mu} \left( \frac{\eta_3 \left(\xi^2 + \gamma^2 - \eta_1^2\right)}{\left(\xi^2 + \gamma^2 + \eta_1^2\right)^2 - 4\eta_1\eta_3 \left(\xi^2 + \gamma^2\right)} \right) \frac{\sin \xi a \sin \gamma b}{ab\xi\gamma}, \tag{4}$$

where $\eta_1 = -\sqrt{\xi^2 + \gamma^2 - \omega^2/v_s^2}$, $\eta_3 = -\sqrt{\xi^2 + \gamma^2 - \omega^2/v_p^2}$; for $\Re(\eta_1) \leq 0$ and $\Re(\eta_3) \leq 0$, $v_p^2 = (\lambda + 2\mu)/\rho$, $v_s^2 = \mu/\rho$; with $v_p$ and $v_s$ being the compressional and shear wave speeds respectively, $\lambda$ and $\mu$ the Lamé constants and $\rho$ the soil density. For a layered ground, however, $\breve{G}(\xi, \gamma, \omega)$ is calculated using the dynamic stiffness method [13].

It is intended here to formulate a dynamic stiffness matrix to allow for interaction between $N$ rectangular strips onto which the track will be coupled. The coupling will be done along the line $y = 0, z = 0$. Hence, the inverse Fourier transform of the Green's function from $\gamma$ to $y$, at the point $y = 0$, can be calculated as

$$\tilde{G}(\xi, y = 0, \omega) = \frac{1}{\pi} \int_0^\infty \breve{G}(\xi, \gamma, \omega) \mathrm{d}\gamma. \tag{5}$$

Equation (5) makes use of the symmetry in the $\gamma$ domain by accounting only for the positive wavenumbers.

The displacement of a point on the ground within the jth strip, whose centre is located at a distance $x_j$ from the $x-$origin, can be calculated as the superposition of the displacements of that point due to the individual excitation at all strips, with their centres located at $x_i$ from the origin. This can be obtained using the inverse Fourier transform from $\xi$ to $x$, at point $x_j$, also utilising symmetry in the $\xi-$domain, as follows

$$\hat{U}_{g_j}(x_j, y = 0, \omega, \tau) = \frac{\mathrm{e}^{-\mathrm{i}\omega\tau}}{\pi} \sum_{i=1}^{N} \int_0^\infty \tilde{G}(\xi, y = 0, \omega) \cos(\xi(x_j - x_i)) \mathrm{d}\xi \tag{6}$$

Let $\Delta_{i,j} = x_j - x_i$, where $x_i = id$ and $x_j = jd$, for $j = 1, \ldots, N$. Additionally, let

$$\hat{G}(\Delta_{i,j}, y = 0, \omega) = \frac{1}{\pi} \int_0^\infty \tilde{G}(\xi, y = 0, \omega) \cos(\xi \Delta_{i,j}) \mathrm{d}\xi \tag{7}$$

be the transfer function of a point at the centre of strip $j$, that is at a distance $\Delta_{i,j}$ from the centre of strip $i$, due to an impulse at strip $i$.

Equation (6) can be formulated for all the strips and the resulting system of equations can be written in matrix form as

$$\hat{\mathbf{U}}_g(\omega) = \hat{\mathbf{G}}(\omega) \hat{\mathbf{F}}_g(\omega), \tag{8}$$

where $\hat{\mathbf{G}}(\omega)$ is an $N \times N$ flexibility matrix of the form

$$\hat{\mathbf{G}}(\omega) = \begin{bmatrix} \hat{G}(0) & \hat{G}(-d) & \cdots & \hat{G}(-(N-2)d) & \hat{G}(-(N-1)d) \\ \hat{G}(d) & \hat{G}(0) & \cdots & \hat{G}(-(N-3)d) & \hat{G}(-(N-2)d) \\ \vdots & \vdots & \ddots & \vdots & \vdots \\ \hat{G}((N-2)d) & \hat{G}((N-3)d) & \cdots & \hat{G}(0) & \hat{G}(-d) \\ \hat{G}((N-1)d) & \hat{G}((N-2)d) & \cdots & \hat{G}(-d) & \hat{G}(0) \end{bmatrix}.$$

and $\hat{\mathbf{F}}_g$ is an $N \times 1$ vector with elements being $\mathrm{e}^{-\mathrm{i}\omega\tau}$.

Finally, the dynamic stiffness matrix $\hat{\mathbf{K}}_g(\omega)$ of the half-space due to the interaction between the strips can be obtained as

$$\hat{\mathbf{K}}_g(\omega) = \left[\hat{\mathbf{G}}(\omega)\right]^{-1} = \begin{bmatrix} \hat{K}_{1,1} & \cdots & \hat{K}_{1,n} \\ \vdots & \ddots & \vdots \\ \hat{K}_{n,1} & \cdots & \hat{K}_{n,n} \end{bmatrix}. \tag{9}$$

## 3. Frequency independent lumped parameter model of the ground

In this section, the process of formulating a lumped parameter model to represent approximately each component $i, j$ of the dynamic stiffness matrix in Eq. (9) will be described. The matrix structure of the complete lumped parameter model equivalent to Eq. (9) will be given and a check of its accuracy will also be carried out.

### *3.1. Rational fraction form of the dynamic stiffness terms*

Suppose that each term $\hat{K}_{i,j}$ of Eq. (9) can be represented in discrete form as the sum of its singular and regular parts. The singular part $\hat{K}^s_{i,j}(\mathrm{i}\omega) = K_0(k_\infty + \mathrm{i}\omega c_\infty)$ describes its asymptotic value at high frequencies, where $k_\infty$ and $c_\infty$ are the high frequency stiffness and damping respectively and $K_0$ is the static stiffness. The remaining regular part is denoted $\hat{K}^r_{i,j}(\mathrm{i}\omega)$. Note that complex frequency notation has been used for equivalence with the Laplace variable. It is assumed that the regular part, $\hat{K}^r_{i,j}(\mathrm{i}\omega)$ can be represented by a rational fraction in which the polynomial in the

numerator has degree $M-1$ and the one in the denominator has degree $M$ as follows

$$\hat{K}^r_{i,j}(\mathrm{i}\omega) = K_0 \frac{1 + p_1(\mathrm{i}\omega) + p_2(\mathrm{i}\omega)^2 + \cdots + p_{M-1}(\mathrm{i}\omega)^{M-1}}{1 + q_1(\mathrm{i}\omega) + q_2(\mathrm{i}\omega)^2 + \cdots + q_M(\mathrm{i}\omega)^M}, \tag{10}$$

where $p_i$ and $q_i$ are the $2M-1$ unknown real coefficients to be determined by numerical curve fitting. The static stiffness $K_0$ is dropped in the derivations to follow, but the dynamic stiffness components should now be considered as being normalised by it.

Alternatively Eq. (10) can be represented as the following partial fraction expansion

$$\hat{K}^r_{i,j}(\mathrm{i}\omega) = \sum_{l=1}^{M} \frac{A_l}{\mathrm{i}\omega - s_l}, \tag{11}$$

where $s_l$ and $A_l$ are the poles and corresponding residues of $\hat{K}^r_{i,j}(\mathrm{i}\omega)$. For a stable system each $s_l$ should have a negative real part. This condition can be achieved by adopting an iterative procedure in the curve fitting routine. The poles and residues of $\hat{K}^r_{i,j}(\mathrm{i}\omega)$ can be all real, all complex conjugate pairs or a combination of these. A real pole results in a first-order term with corresponding real coefficients, whereas a pair of complex conjugate poles, when added together forms a second-order term with real coefficients. For $J$ complex conjugate pairs and the remaining $M-2J$ real poles, the dynamic stiffness for the generalised lumped parameter model can be written in the following form that includes all the sub components

$$\hat{K}_{i,j}(\mathrm{i}\omega) = k_\infty + \mathrm{i}\omega c_\infty + \sum_{l=1}^{J} \frac{\beta_{1l}\mathrm{i}\omega + \beta_{0l}}{(\mathrm{i}\omega)^2 + \alpha_{1l}\mathrm{i}\omega + \alpha_{0l}} + \sum_{l=1}^{M-2J} \frac{A_l}{\mathrm{i}\omega - s_l}, \tag{12}$$

The coefficients of the second-order term are as follows

$$\alpha_{0l} = \prod_{i=j}^{j+1} s_i, \quad \alpha_{1l} = -\sum_{i=j}^{j+1} s_i, \quad \beta_{0l} = -(A_j s_{j+1} + A_{j+1} s_j), \quad \beta_{1l} = \sum_{i=j}^{j+1} A_i, \tag{13}$$

where $j \in \{1, 3, \cdots, 2J-1\}$ and $j+1$ form a pair of complex conjugate poles and of corresponding residues at those poles.

*3.2. Generalised lumped parameter model*

Using the poles and residues obtained from the partial fraction expansion, each component of the lumped parameter model can be formed. Figure 2(a) shows the generalised lumped parameter model representing the force-displacement relationship between nodes $i$ and $j$ for $i \neq j$ (i.e. for coupling terms). This model differs from that presented in [24] in that it contains masses in addition to springs and dashpots and is formulated so that coupling terms can be modelled, and not only diagonal terms. Figure 2(b) shows the corresponding lumped parameter model for the diagonal terms, i.e. for $i = j$, in which node $i$ is connected to a fixed support. In both cases, the components marked (I), (II) and (III) correspond to the contributions of the singular term, the first-order terms and second-order terms of the regular part respectively.

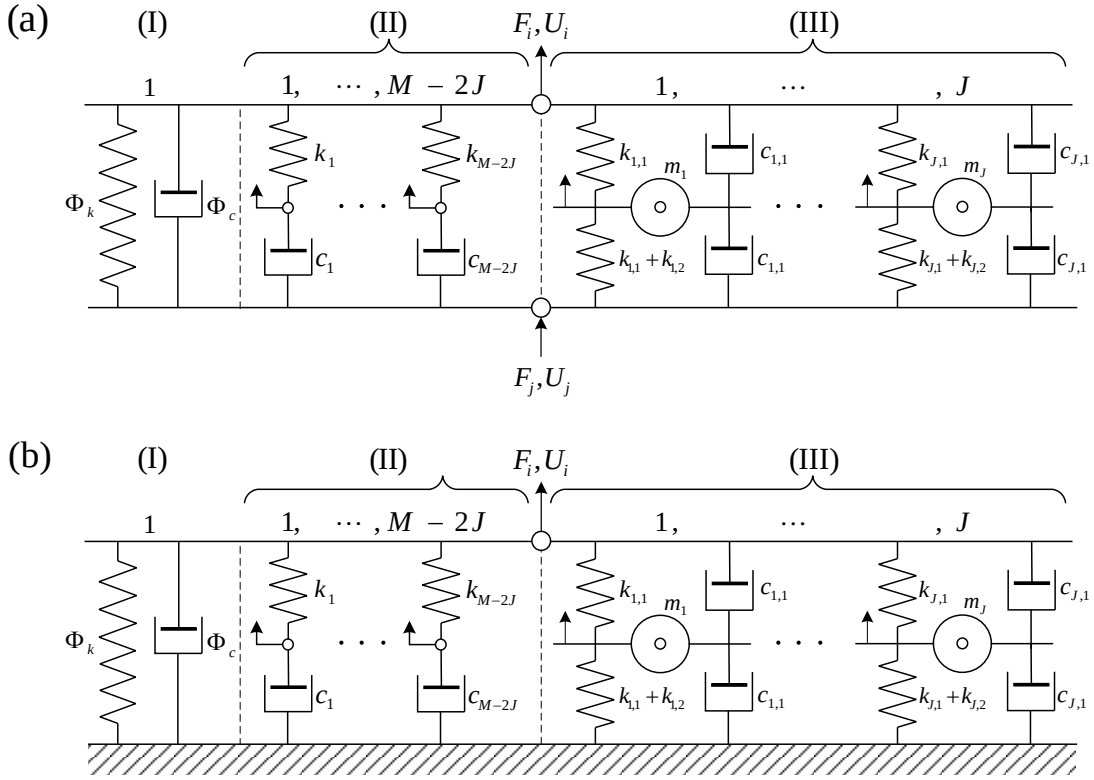


Figure 2: Lumped parameter models for the ground describing of the force-displacement relationship for (a) coupling terms and (b) diagonal terms of the dynamic stiffness matrix

The singular and regular parts of the dynamic stiffness in Eq. (12) are obtained by polynomial

division, starting with an improper rational fraction with numerator of degree $M+1$ and denominator of degree $M$. This gives a quotient, $k_\infty + \mathrm{i}\omega c_\infty$ and a remainder that corresponds to the regular part as defined in Eq. (10).

The dynamic stiffness of the lumped parameter model is given in the frequency domain by

$$\hat{K}_{i,j}^{\mathrm{lpm}}(\mathrm{i}\omega) = k_\infty + \mathrm{i}\omega c_\infty + \sum_{l=1}^{J} \frac{2\dfrac{c_{l,1}\left(c_{l,1}^2 - k_{l,1}m_l\right)}{m_l^2}\mathrm{i}\omega + \dfrac{\left(2k_{l,1}+k_{l,2}\right)c_{l,1}^2 - k_{l,1}^2 m_l}{m_l^2}}{(\mathrm{i}\omega)^2 + 2\dfrac{c_{l,1}}{m_l}\mathrm{i}\omega + \dfrac{2k_{l,1}+k_{l,2}}{m_l}} + \sum_{l=1}^{M-2J} \frac{\dfrac{-k_l^2}{c_l}}{\mathrm{i}\omega + \dfrac{k_l}{c_l}}. \quad (14)$$

The coefficients of the first and second order terms are obtained by comparing Eqs. (12) and (14) as follows

$$k_l = \frac{A_l}{s_l}, \quad c_l = -\frac{A_l}{s_l^2}, \quad k_{l,1} = \frac{m_l\alpha_{1l}^2}{4} - \frac{\beta_{1l}}{\alpha_{1l}}, \quad k_{l,2} = m_l\alpha_{0l} - 2k_{l,1}, \quad c_{l,1} = \frac{m_l\alpha_{1l}}{2}, \quad (15)$$

where $m_l$ is calculated by solving the following equations

$$(\alpha_{1l}^4 - 4\alpha_{0l}\alpha_{1l}^2)m_l^2 + (16\beta_{0l} - 8\alpha_{1l}\beta_{1l})m_l + 16\frac{\beta_{1l}^2}{\alpha_{1l}^2} = 0, \quad (16)$$

with real $m_l$ obtained when $\alpha_{0l}\beta_{1l}^2 - \alpha_{1l}\beta_{0l}\beta_{1l} + \beta_{0l}^2 \geq 0$.

In the time domain, the force-displacement relationship of the generalised lumped parameter model can be expressed in matrix form as

$$\left\{F_{i,j}^{\mathrm{lpm}}\right\} = \left[M_{i,j}^{\mathrm{lpm}}\right]\left\{\ddot{U}_{i,j}^{\mathrm{lpm}}\right\} + \left[C_{i,j}^{\mathrm{lpm}}\right]\left\{\dot{U}_{i,j}^{\mathrm{lpm}}\right\} + \left[K_{i,j}^{\mathrm{lpm}}\right]\left\{U_{i,j}^{\mathrm{lpm}}\right\}, \quad (17)$$

where

$$M_{i,j}^{\mathrm{lpm}} = \mathrm{diag}\left\{0 \quad 0 \quad \cdots \quad 0 \quad m_1 \quad \cdots \quad m_J \quad 0\right\},$$

$$C_{i,j}^{\text{lpm}} = \begin{bmatrix} \Phi_c & & & & -c_{1,1} & \cdots & -c_{J,1} & -c_\infty \\ & c_1 & & & & & & -c_1 \\ & & \ddots & & & & & \vdots \\ & & & c_{M-2J} & & & & -c_{M-2J} \\ -c_{1,1} & & & & 2c_{1,1} & & & -c_{1,1} \\ \vdots & & & & & \ddots & & \vdots \\ -c_{J,1} & & & & & & 2c_{J,1} & -c_{J,1} \\ -c_\infty & -c_1 & \cdots & -c_{M-2J} & -c_{1,1} & \cdots & -c_{J,1} & \Phi_c + \sum_{l=1}^{M-2J} c_l \end{bmatrix},$$

$$K_{i,j}^{\text{lpm}} = \begin{bmatrix} \Phi_k & -k_1 & \cdots & -k_{M-2J} & -k_{1,1} & \cdots & -k_{J,1} & \Psi_k \\ -k_1 & k_1 & & & & & & \\ \vdots & & \ddots & & & & & \\ -k_{M-2J} & & & k_{M-2J} & & & & \\ -k_{1,1} & & & & 2k_{1,1} + k_{1,2} & & & -k_{1,1} \\ \vdots & & & & & \ddots & & \vdots \\ -k_{J,1} & & & & & & 2k_{J,1} + k_{J,2} & -k_{J,1} \\ \Psi_k & & & & -k_{1,1} & \cdots & -k_{J,1} & \Phi_k - \sum_{l=1}^{M-2J} k_l \end{bmatrix},$$

and $\left\{U_{i,j}^{\text{lpm}}\right\}^T = \left\{u_i, \quad u_1, \quad \cdots, \quad u_{M-2J}, \quad u_{M-2J+1}, \cdots \quad \cdots \quad, u_{M-J}, u_j\right\}$.
In the expressions for $K_{i,j}^{\text{lpm}}$ and $C_{i,j}^{\text{lpm}}$ for $i \neq j$, representing an off-diagonal term, we have

$$\Phi_k = k_\infty + \sum_l^J \left(k_{l,1} + \frac{c_{l,1}^2}{m_l}\right), \quad \Psi_k = -k_\infty + \sum_{l=1}^{M-2J} k_l - \sum_l^J \frac{c_{l,1}^2}{m_l}, \quad \Phi_c = c_\infty + \sum_{l=1}^J c_{l,1} \tag{18}$$

For a diagonal term, i.e. $i = j$, the last row and column are eliminated as node $i$ is connected to a fixed support. In this case,

$$\Phi_k = k_\infty + \sum_l^J \frac{c_{l,1}^2}{m_l}, \quad \Phi_c = c_\infty. \tag{19}$$

The lumped parameter model in Fig. 2 is not unique. Other alternative arrangements are possible for both the first- and second-order terms. For example, the spring-dashpot-mass model shown in Fig. 4 of reference [17] can be used instead of model component (II) in Fig. 2. However

this model component offers no real benefit over the current one as it also has one internal dof. In fact it has been found in [17, 18] and observed also in this work that models based only on spring-dashpot elements perform better than their spring-dashpot-mass counterparts. The model component in (III), on the other hand, halves the number of internal dof resulting from second-order poles and residues when compared with the model based only on spring-dashpot elements in Fig. 3 of reference [17].

Additionally, it would be possible to add two first-order real roots to form a second-order one which can be modelled by component (III) of the lumped parameter model. Although this is similar to the addition of a pair of complex conjugate terms, it has not been possible to obtain real values for $m_l$ in all cases. It has been observed from a frequency domain analysis that when complex masses are included in the lumped parameter model, the resulting solutions exhibit spurious oscillations about the target solutions. Furthermore, only mass components with real coefficients can be accurately represented in a time domain analysis. For these reasons, all first-order real roots have been modelled individually using component (II) of the lumped parameter model.

### *3.3. Modelled dynamic stiffness*

The individual terms of the dynamic stiffness matrix in Eq. (9) can be represented using separate lumped parameter models. In order to model the force-displacement relationship of the system correctly, modelling units should be formulated and these are different for diagonal and off-diagonal terms. According to Wolf [17], each off-diagonal term, $\hat{K}_{i,j}(\mathrm{i}\omega)$ directly forms a modelling unit that represents the force-displacement relationship between dof $i$ and $j$. This relationship can be obtained by enforcing the displacement $u_i$ with $u_j = 0$ for $j \neq i$, so that there is a reaction force $R_j = \hat{K}_{j,i}(\mathrm{i}\omega)u_i(\mathrm{i}\omega)$ at node $j$. Additionally, this loading condition will also induce a reaction force, $R^i_j$, at node $i$ due to its connection to node $j$, and this should be accounted for when modelling a diagonal term.

For the diagonal term, the resulting interaction force is given by

$$R_i^{\mathrm{m}}(\mathrm{i}\omega) = R_i(\mathrm{i}\omega) - \sum_{j=1}^{N} R_i^j(\mathrm{i}\omega)(1 - \delta_{ji}) \tag{20}$$

where

$$R_i(\mathrm{i}\omega) = \hat{K}_{i,i}(\mathrm{i}\omega)u_i(\mathrm{i}\omega), \tag{21}$$

$\delta_{ji}$ is the Kronecker delta, and the superscript 'm' signifies a modelled unit.

The definition of $R_i^j(\mathrm{i}\omega)$ depends on the nature of the components that make up the lumped parameter model. For a lumped parameter model consisting of only springs and dashpots

$$R_i^j(\mathrm{i}\omega) = -R_j(\mathrm{i}\omega) = -\hat{K}_{j,i}(\mathrm{i}\omega)u_i(\mathrm{i}\omega). \tag{22}$$

Substituting Eqs. (21)-(22) into Eq. (20) and taking $R_i^{\mathrm{m}}(\mathrm{i}\omega) = \hat{K}_{i,i}^{\mathrm{m}}(\mathrm{i}\omega)u_i(\mathrm{i}\omega)$, results in the modelled dynamic stiffness for a diagonal term as

$$\hat{K}_{i,i}^{\mathrm{m}}(\mathrm{i}\omega) = \hat{K}_{i,i}(\mathrm{i}\omega) + \sum_{j=1}^{N} \hat{K}_{j,i}(\mathrm{i}\omega)(1 - \delta_{ji}) \tag{23}$$

Equation (23) is valid for the singular part and first-order terms of the regular part of the dynamic stiffness.

On the other hand, when the lumped parameter model consists of masses in addition to springs and dashpots, the interaction force changes. Considering the lumped parameter model component (III) in Fig. 2 for second-order terms, we have [17]

$$R_i^j(\mathrm{i}\omega) = R_j(\mathrm{i}\omega) + \sum_{l=1}^{J} (k_{l,1} + \mathrm{i}\omega c_{l,1})u_i(\mathrm{i}\omega), \tag{24}$$

Again, substitution of Eq. (24) into Eq. (20), together with the expressions for $R_i(\mathrm{i}\omega)$, $R_j(\mathrm{i}\omega)$ and $R_i^{\mathrm{m}}(\mathrm{i}\omega)$, results in the following modelled dynamic stiffness for a diagonal term with a spring-dashpot-mass model

$$\hat{K}_{i,i}^{\mathrm{m}}(\mathrm{i}\omega) = \hat{K}_{i,i}(\mathrm{i}\omega) - \sum_{j=1}^{N} \left( \hat{K}_{j,i}(\mathrm{i}\omega) + \sum_{l=1}^{J} (k_{l,1} + \mathrm{i}\omega c_{l,1}) \right) (1 - \delta_{ji}) \tag{25}$$

Note that Eqs. (23) and (25) respectively apply only to the corresponding portions of the dynamic stiffness term that are modelled with spring-dashpot components, i.e. (I) and (II), and

spring-dashpot-mass components in (III), and not to the total dynamic stiffness. The total modelling unit is therefore a sum of contributions of Eqs. (23) and (25).

### *3.4. Implementation of the lumped parameter model*

Due to the symmetric structure of the dynamic stiffness matrix in Eq. (9), the number of unique terms that exist in it, and hence the number of terms to be modelled, can be calculated as

$$n = \begin{cases} \sum_{k=1}^{(N+1)/2} (2k-1) & \text{if } N \text{ is odd} \\ \sum_{k=1}^{N/2} 2k & \text{if } N \text{ is even} \end{cases} \tag{26}$$

Furthermore, the number of coupling terms is the sum of all elements on one side of the principal diagonal, i.e.

$$n_c = \sum_{k=1}^{N-1} N - k \tag{27}$$

The derivation of the lumped parameter model for each $\hat{K}_{i,j}$ begins with the rational fraction form. The *invfreqs* function in MATLAB is used to perform the frequency domain curve fitting to obtain the coefficients of the singular and regular parts, while the *residue* function is used to obtain the poles and residues of the regular part. Alternatively, the curve-fitting routine reported by Andersen [25] could be adopted. The *invfreqs* function has iterative capabilities in order to improve the chances of obtaining a stable fit (i.e. poles with negative real parts), with each iteration involving the minimisation of a weighted squared residual objective function. A large enough number should be specified as a limit for the number of iterations that can be performed.

In addition to the iterative process of the *invfreqs* function, an iterative routine is employed to obtain the appropriate order of polynomials necessary to formulate an accurate lumped parameter model. This routine is summarised in the following steps:

1. Choose an initial value for the order of the denominator polynomial, $M$, and perform the curve fitting to obtain $k_\infty$, $c_\infty$, $p_i$ and $q_i$. The iteration of the *invfreqs* function will continue until a stable solution is obtained. If the maximum iteration is reached without obtaining a stable solution, the fitted curve will not satisfy the convergence criterion in step 5 and an increased $M$ value will then be tested.

2. Using the poles and residues computed from the coefficients of the regular part, calculate the properties of the individual elements of the lumped parameter model as defined in Eqs. (15)-(16).

3. *If* $i = j$ derive the modelled dynamic stiffness by separately applying Eq. (23) to the spring-dashpot components, i.e. (I) and (II), and Eq. (25) to (III) of Fig. 2. Subsequently, repeat steps 1-2 and continue to step 4.

   *else* continue to step 4.

4. At each frequency, compare the total dynamic stiffness of the lumped parameter model, i.e. Eq. (14), with the input dynamic stiffness term, or in the case of a diagonal term, with the modelled dynamic stiffness. The following coefficient of determination

$$R^2 = 1 - \frac{\sum_{r=1}^{n_\omega} \left( |\hat{K}_{i,j}^{\mathrm{m},r}| - |\hat{K}_{i,j}^{\mathrm{lpm},r}| \right)^2}{\sum_{r=1}^{n_\omega} \left( |\hat{K}_{i,j}^{\mathrm{m},r}| - \frac{1}{n_\omega} \sum_{r=1}^{n_\omega} |\hat{K}_{i,j}^{\mathrm{m},r}| \right)^2}, \tag{28}$$

   with $n_\omega$ being the number of frequency points, is used to indicate how well the lumped parameter model fits the dynamic stiffness data, with an $R^2$ value of 1 indicating perfect fit. The error estimate applied only to the magnitude of the dynamic stiffness has been found to work better than one applied either to the real and imaginary parts together or the magnitude and phase together.

5. *If* $R^2 < 1 - \varepsilon$, where $\varepsilon$ is a predefined tolerance parameter, choose $M = M + 1$. Repeat steps 1-4 until $R^2 \geq 1 - \varepsilon$ is achieved.

## 4. Numerical application of the lumped parameter model

In this section, a numerical example is presented to demonstrate the use of the lumped parameter model in studying the dynamic interaction between massless strips on a half-space. Other examples of the use of lumped parameter models can be found in [26, 27, 28], where the dynamic soil-structure interaction of a surface footing and suction caisson embedded in the ground are considered.

The following parameters are used for the ground: $\rho = 1800$ kg/m$^3$, $v_s = 245$ m/s, $v_p = 750$ m/s and damping ratio of 0.05. In addition, each strip has dimensions $2a = 0.6$ and $2b = 2.7$ m with spacing $d = 0.6$ m (see Fig. 1).

### *4.1. Frequency domain curve fitting*

The vertical dynamic stiffness given in Eq. (9) is computed using the semi-analytical model for three strips arranged symmetrically about $y = 0$ and along the $x-$ axis such that the distance between the centres of two consecutive strips is $2a$. The computation is done for 128 logarithmically spaced frequencies between 0.5 and 500 Hz. The frequency discretisation does not affect the accuracy of the computed dynamic stiffness matrix but rather the accuracy of the resulting lumped parameter model. 128 log-spaced points represent accurately the dynamic stiffness components, capturing the peaks and dips that exist within the frequency range of interest. Log spacing has been used to act as a weighting function in the curve fitting procedure. Due to singularity of the method at 0 Hz, the minimum frequency considered is not zero. In the computation, 512 linearly spaced wavenumber samples between 0 and $10\pi$ rad/m are used for both the $x-$ and $y-$ directions. A finer discretisation grid of 1024 points was also checked and found not to significantly change the results within the frequency range of interest.

Due to symmetry, the number of unique terms in the $3 \times 3$ dynamic stiffness matrix that need to be modelled is $n = 4$, i.e. $\hat{K}_{1,1} = \hat{K}_{3,3}$, $\hat{K}_{1,2} = \hat{K}_{2,1} = \hat{K}_{2,3} = \hat{K}_{3,2}$, $\hat{K}_{1,3}$ and $\hat{K}_{2,2}$. The routine outlined in the previous section is used to formulate the lumped parameter model. In order to obtain the static stiffness, which should be purely real, each dynamic stiffness term to be modelled is extrapolated from 0.5 Hz to 0 Hz, using the gradient of its magnitude around 0.5 Hz. The gradient is calculated using the central difference method. Also each term of the dynamic stiffness matrix is normalised by its static stiffness, $K_0$, and a non-dimensional frequency, $\bar{\omega} = \omega a / v_s$, is introduced before performing the frequency domain curve fitting, with $\bar{\omega} = 1$ corresponding to $\approx$130 Hz in this example.

Figure 3 shows the dynamic stiffness terms as calculated from Eq. (9) and the rational fraction fitting from which the lumped parameter model is obtained for each modelling unit. The off-diagonal terms are fitted directly as each one forms a modelling unit. The semi-analytical stiffness

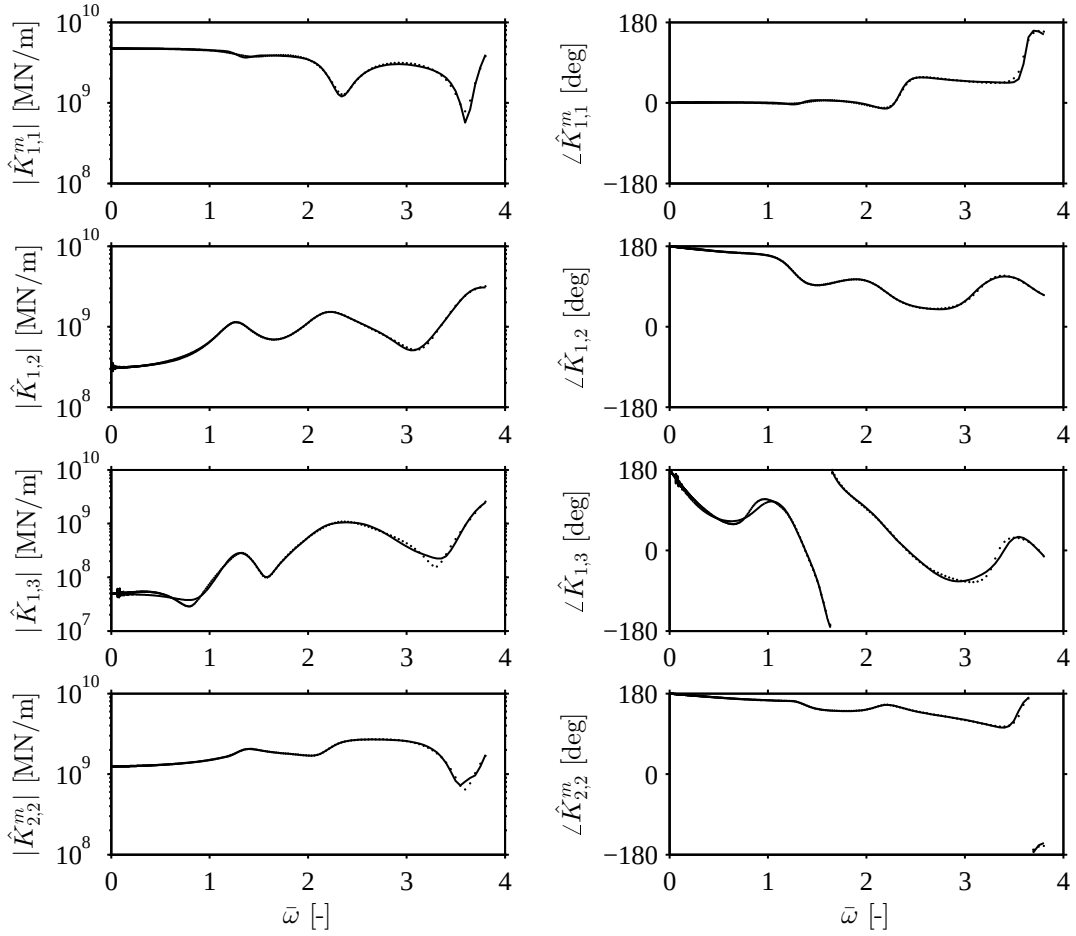


Figure 3: Magnitude and phase of the terms of the vertical dynamic stiffness matrix plotted against non-dimensional frequency, $\bar{\omega}$ for 3 strips at the surface of a half-space. Comparison between the semi-analytical —— and lumped parameter models ·····

terms in this case are closely matched using rational fractions with $M = 7$ and 8 for $\hat{K}_{1,2}$ and $\hat{K}_{1,3}$ respectively. For the diagonal terms, however, the modelled unit is given by a superposition of Eqs. (23) and (25), with the former used for the spring-dashpot components and the latter for the spring-dashpot-mass components. Rational fractions with $M = 6$ and 7 are fitted to $\hat{K}^m_{1,1}$ and $\hat{K}^m_{2,2}$ respectively. $\hat{K}^m_{1,1}$ differs from $\hat{K}^m_{2,2}$ because they are formed from different elements of the dynamic stiffness matrix. For example, applying only Eq. (23), it is easy to see that $\hat{K}^m_{1,1} = K_{1,1} + K_{1,2} + K_{1,3}$, whereas $\hat{K}^m_{2,2} = K_{2,2} + 2K_{2,1}$.

In all cases, the tolerance parameter $\varepsilon$ was set as 0.005, with the iteration beginning at $M = 3$. The tolerance can be made less stringent, leading to lower values of $M$ at the end of the iterations.

### *4.2. Lumped parameter model*

Table 1 gives the values for the respective components of the lumped parameter model derived from the poles and residues of the rational fraction fitting.

Table 1: Coefficients of the components of the lumped parameter model

| Stiffness | Lumped parameter model components | | | | | | | | | |
|---|---|---|---|---|---|---|---|---|---|---|
| | $J$ | $K_0$ | $k_\infty$ | $c_\infty$ | $k_l$ | $c_l$ | $k_{l,1}$ | $k_{l,2}$ | $c_{l,1}$ | $m_l$ |
| $\hat{K}^{\mathrm{m}}_{1,1}$ | 3 | $4.708\times10^{9}$ | 0.843 | 0.285 | | | 1.885 | -25.625 | -0.452 | -1.374 |
| | | | | | | | 0.462 | -2.292 | -0.092 | -0.256 |
| | | | | | | | 0.160 | -0.851 | -0.088 | -0.263 |
| $\hat{K}^{\mathrm{m}}_{1,2}$ | 3 | $-3.098\times10^{8}$ | -53.253 | 3.125 | -51.534 | -3.892 | -6.190 | -13.888 | -0.660 | -1.967 |
| | | | | | | | -0.212 | 0.371 | -0.003 | -0.011 |
| | | | | | | | -1.352 | 0.028 | -0.277 | -1.646 |
| $\hat{K}^{\mathrm{m}}_{1,3}$ | 3 | $-4.894\times10^{7}$ | 26.981 | -2.418 | 41.548 | 20.957 | 67.285 | 889.631 | 11.754 | 68.289 |
| | | | | | -13.526 | -17.144 | 24.956 | -156.866 | -6.117 | -19.768 |
| | | | | | | | 8.246 | -73.004 | -4.621 | -31.082 |
| $\hat{K}^{\mathrm{m}}_{2,2}$ | 3 | $-1.249\times10^{9}$ | 25.098 | -2.135 | 23.636 | 1.948 | 3.265 | 7.832 | 0.624 | 1.090 |
| | | | | | | | -0.053 | 0.131 | 0.001 | 0.005 |
| | | | | | | | -0.418 | -1.608 | -0.214 | -1.265 |

Figure 4 shows a schematic of the lumped parameter model. The diagonal terms are connected to a fixed support while the coupling terms connect one node to another. Due to symmetry, the first and last diagonal terms are equal. Also, the coupling between nodes 1 and 2 is the same as that between nodes 2 and 3. The lumped parameter model for each unit becomes more complicated as $j$ increases; in this case the model for $\hat{K}^{\mathrm{m}}_{1,3}$ has one more internal dof than that for $\hat{K}^{\mathrm{m}}_{1,2}$.

### *4.3. Results for the lumped parameter model*

Figure 5(a-b) shows the magnitude and phase of the displacement of the nodes plotted against excitation frequency for a distributed unit load acting at strip 2. The corresponding results for

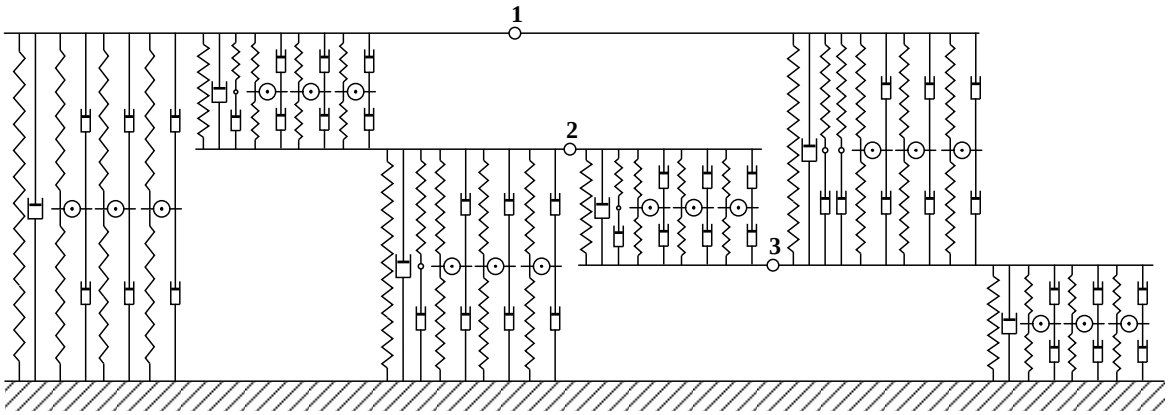


Figure 4: Lumped parameter model for the interaction between 3 strips acting on a half-space

a load acting at strip 1 are shown in Fig. 5(c-d). In both cases, the lumped parameter model representation is compared with the semi-analytical half-space solution.

For the case in Fig. 5(a-b), the load acting at strip 2 results in a symmetric system such that $u_1 = u_3$. On the other hand, a non-symmetric case is obtained when the load acts at strip 1, resulting in different displacements for all points, with decreasing amplitudes away from the load. In both cases, it is evident that the lumped parameter model is in good agreement with the semi-analytical solution.

### *4.4. Extension to track/ground coupling*

The example presented above demonstrates the accuracy of the lumped parameter model as a possible alternative to the direct modelling of the ground (using either finite or boundary elements). The full interaction between the strips has been considered.

When coupling a railway track to the ground, the number of strips required is equivalent to the number of sleepers, $N_s$, included in the track model. However, considering that a railway track is an infinitely long structure in which $N_s$ can be quite large, it is reasonable to expect, at least for engineering purposes, that the through-ground coupling between strips will extend only to a finite region along the track. Therefore each strip will be coupled only to a maximum of $N_c$ others on either side of its location, where $N_c < N_s$. Hence, the dynamic stiffness matrix computed in

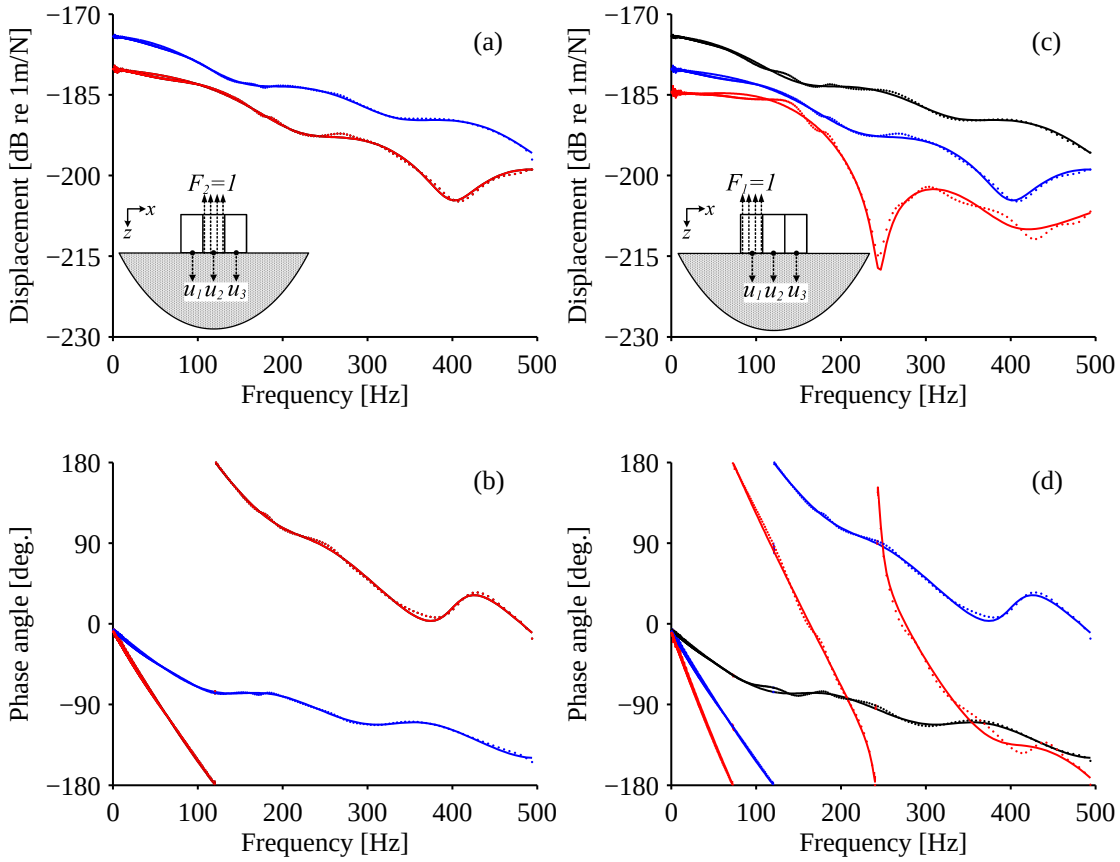


Figure 5: Magnitude and phase of the vertical nodal displacements at the surface of a half-space for $N = 3$ strips, when a distributed load acts at (a-b) strip 2 and (c-d) strip 1. Comparison between the semi-analytical ($u_1$:——, $u_2$:——, $u_3$:——) and lumped parameter models ($u_1$:· · · · · ·, $u_2$:· · · · · ·, $u_3$:· · · · · ·)

Eq. (9) only needs to have dimensions $(2N_c + 1) \times (2N_c + 1)$ regardless of the magnitude of $N_s$. Furthermore, within this matrix only dynamic stiffness terms that are located a maximum of $N_c$ from the principal diagonal are required with the others disregarded. By mapping this matrix onto an $N_s \times N_s$ one, a banded matrix is formed with upper and lower bandwidths equal to $N_c$.

In the actual implementation, the approximate lumped parameter model is obtained for the unique terms of the $2N_c + 1 \times 2N_c + 1$ matrix and mapped on to the $N_s \times N_s$ matrix in order to form the global lumped parameter model of the ground. The effect of $N_c$ will be investigated in the following sections.

## 5. Space-time domain coupling of track and ground

### *5.1. Model description*

Figure 6 shows a model of a ballasted railway track formulated in the space-time domain using the FE method. For the purpose of demonstrating the use of the mixed formulation, a linear track model is used in the current work, although the method has the potential to deal with nonlinear track elements such as railpads, which indeed is the motivation for its development. The track model consists of a rail that is discretely supported on sleepers via railpads, the sleepers are in turn supported by a layer of ballast and the entire track system rests on the ground. Due to symmetry about the centre line of the track, only one-half of the track (i.e. one rail) is considered.

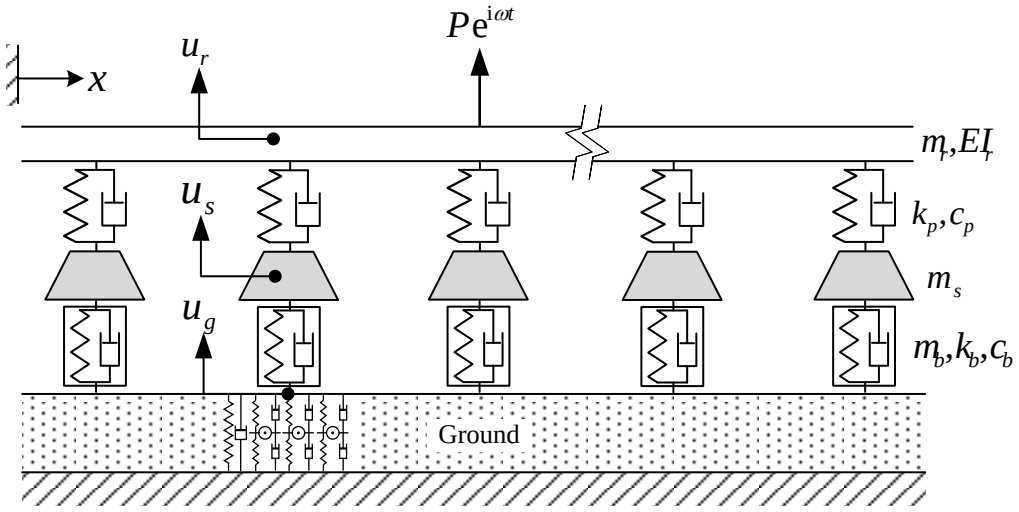


Figure 6: A 2D view of the track/ground model. The ballast has been represented as concentrated at the sleeper and ground nodes

The rail is modelled as an Euler-Bernoulli beam of mass per unit length, $m_r$, and bending stiffness, $EI$. The railpads are modelled as springs and dashpots having stiffness and damping, $k_p$ and $c_p$ respectively. The sleepers are modelled as lumped masses, $m_s$, allowing only for vertical translations. At each sleeper position, the ballast is modelled as having stiffness $k_b$ and damping $c_b$, and a mass, $m_b$, consistently distributed between the sleeper and ground nodes. The lumped parameter model formulated in Section 3 to represent the ground is coupled to the the lower nodes.

Through-ground coupling is also accounted for, as described in Section 4.4. The excitation of the track/ground system is due to a stationary harmonic load of amplitude $P$ and angular frequency $\omega$ acting at the centre of the rail.

It should be pointed that while this model may be adequate for studying ground vibration within the dominant frequency range of up to 250 Hz, its accuracy at higher frequencies may be impaired by several factors. Firstly, the Euler-Bernoulli beam theory limits the modelling to approximately 500 Hz, beyond which shear deformation of the rail becomes important. Furthermore, at higher frequencies the ballast cannot be accurately represented as point springs and the sleepers behave as flexible beams.

### *5.2. Equation of motion of the track/ground model*

The differential equation for the coupled track/ground model is given by

$$\begin{bmatrix} \mathbf{M}_r & \mathbf{0} & \mathbf{0} \\ \mathbf{0} & \mathbf{M}_s + \mathbf{M}_b^{ss} & \mathbf{M}_b^{sg} \\ \mathbf{0} & \mathbf{M}_b^{gs} & \mathbf{M}_b^{gg} \end{bmatrix} \begin{Bmatrix} \ddot{\mathbf{U}}_r \\ \ddot{\mathbf{U}}_s \\ \ddot{\mathbf{U}}_g \end{Bmatrix} + \begin{bmatrix} \mathbf{C}_p^{rr} & \mathbf{C}_p^{rs} & \mathbf{0} \\ \mathbf{C}_p^{sr} & \mathbf{C}_p^{ss} + \mathbf{C}_b^{ss} & \mathbf{C}_b^{sg} \\ \mathbf{0} & \mathbf{C}_b^{gs} & \mathbf{C}_b^{gg} \end{bmatrix} \begin{Bmatrix} \dot{\mathbf{U}}_r \\ \dot{\mathbf{U}}_s \\ \dot{\mathbf{U}}_g \end{Bmatrix} + \begin{bmatrix} \mathbf{K}_r + \mathbf{K}_p^{rr} & \mathbf{K}_p^{rs} & \mathbf{0} \\ \mathbf{K}_p^{sr} & \mathbf{K}_p^{ss} + \mathbf{K}_b^{ss} & \mathbf{K}_b^{sg} \\ \mathbf{0} & \mathbf{K}_b^{gs} & \mathbf{K}_b^{gg} \end{bmatrix} \begin{Bmatrix} \mathbf{U}_r \\ \mathbf{U}_s \\ \mathbf{U}_g \end{Bmatrix} = \begin{Bmatrix} \mathbf{F}_r \\ \mathbf{0} \\ -\mathbf{F}_g \end{Bmatrix}, \tag{29}$$

where $\mathbf{M}_{\{\cdot\}}$, $\mathbf{C}_{\{\cdot\}}$, $\mathbf{K}_{\{\cdot\}}$ and $\mathbf{U}_{\{\cdot\}}$ are the global mass, damping and stiffness matrices and displacement vector of the track components indicated by the subscripts, $r$, $s$, $b$ and $g$, for the rail, sleeper, ballast and ground respectively. The superscripts designate cross-coupling between these components. $\mathbf{F}_r$ is the nodal force vector of the rail and contains the the excitation force and $\mathbf{F}_g$ is the interaction force vector at the ballast/ground interface and is given by the global form of Eq. (17). Since the ground displacements are also unknown, direct substitution of $\mathbf{F}_g$ results in a modification to the global mass, damping and stiffness matrices of the track/ground model.

### *5.3. Solution of the coupled equation of motion*

Since the load on the track is assumed to be a stationary harmonic load, and the system is linear, the track and ground will vibrate at the same frequency as the load. It is therefore sufficient to obtain directly the steady-state vibration from

$$\left[-\omega^2 \mathbf{M}^{\mathrm{t/g}} + \mathrm{i}\omega \mathbf{C}^{\mathrm{t/g}} + \mathbf{K}^{\mathrm{t/g}}\right] \left\{\mathbf{U}^{\mathrm{t/g}}\right\} = \left\{\mathbf{F}^{\mathrm{t/g}}\right\}, \tag{30}$$

for the coupled track/ground system, where the superscript 't/g' stands for track/ground. It is also possible to use progressive time integration schemes [29, 30, 31] to solve Eq. (29) when the load is transient, as will be discussed later in Section 8.

The calculated interaction forces at the ballast/ground interface are then used as input to the wavenumber-frequency domain ground model to calculate ground vibration in the far field. This process is described in the next section.

## 6. Calculation of free-field ground vibration

Using the computed steady-state displacements, velocities and accelerations of the sleeper and ground nodes, the complex amplitudes of the interaction forces, $\mathbf{F}_g$ at the ballast/ground interface can be calculated using the global form of Eq. (17).

The non-zero forces of $\mathbf{F}_g$ occur at the ground nodes that are coupled to the sleepers, with the forces at the internal dofs of the lumped parameter model being zero. These non-zero forces are assembled in a new vector, $F_g(x_s, \omega)$ of size $N_s \times 1$, where $x_s$ are the positions of the sleepers relative to $x = 0$. These forces are located at discrete points along the track. For the purpose of performing a Fourier transformation to the wavenumber domain for application to the ground model, it is convenient to convert $F_g(x_s, \omega)$ into a piecewise continuous function, $F'_g(x, \omega)$. This is done using a cubic spline interpolation function at spatial points, $x$, defined so that the Nyquist criterion is satisfied with relation to the wavenumber sampling for the Fourier transformation and subsequent half-space calculations. This conversion also means that the discrete forces should be distributed per unit length of track by dividing by the sleeper spacing.

The spatial Fourier transformation of $F'_g(x, \omega)$ to the wavenumber domain is given by

$$\hat{F}'_g(\xi, \omega) = \int_{-\infty}^{\infty} F'_g(x, \omega) \mathrm{e}^{-\mathrm{i}\xi x} \mathrm{d}x. \tag{31}$$

In the $y-$direction the force is assumed to be uniformly distributed over the width $2b$ of the ballast/ground contact. Transforming to the wavenumber domain in the $y-$direction gives $(\sin \gamma b)/\gamma b$. Hence the complex amplitude of the ground displacement in the wavenumber domain can be ob-

tained as

$$\tilde{U}'_g(\xi,\gamma,\omega) = \breve{G}(\xi,\gamma,\omega)\hat{F}'_g(\xi,\omega)\frac{\sin\gamma b}{\gamma b}, \tag{32}$$

Finally, the corresponding displacement in the space domain is obtained by performing the double inverse Fourier transformation as follows

$$u'_g(x,y,\omega) = \frac{1}{4\pi^2}\int_{-\infty}^{\infty}\int_{-\infty}^{\infty}\breve{G}(\xi,\gamma,\omega)\hat{F}'_g(\xi,\omega)\frac{\sin\gamma b}{\gamma b}\mathrm{e}^{\mathrm{i}(\xi x+\gamma y)}\mathrm{d}\xi\mathrm{d}\gamma. \tag{33}$$

## 7. Results and discussion

In this section, results will be presented to show the validity of the mixed formulation for the prediction of the track dynamic response, interaction forces at the track/ground interface and the free-field ground vibration. In all cases, the FEM solutions including the lumped parameter models are compared with a semi-analytical track/ground model [2]. Table 2 contains the track parameters used in the computations, which apply to half the track with a single rail. The parameters given for the railpad, sleeper and ballast are for each fastener bay. These values are continuously distributed in the semi-analytical model by dividing by the sleeper spacing. For the ground the same parameters as in Section 4 are used.

Table 2: Parameters for the ballasted railway track used in the numerical simulations

| Track components | Parameter | Parameter value |
|---|---|---|
| *Rail* | Mass, $m_r$ | 60.21 kg/m |
| | Bending stiffness, $EI_r$ | 6.4 MN m$^2$ |
| *Railpad* | Stiffness, $k_p$ | 60 MN/m |
| | Damping ratio, $\zeta_p$ | 0.125 |
| *Sleeper* | Mass, $m_s$ | 150 kg |
| | Spacing, $d$ | 0.6 m |
| *Ballast* | Mass, $m_b$ | 522 kg |
| | Stiffness, $k_b$ | 100 MN/m |
| | Damping ratio, $\zeta_b$ | 0.5 |

For the FEM calculation, a 60 m long track is modelled using 200 beam elements, i.e. each

0.3 m long, 101 sleepers, and therefore same number of ground nodes. This length of track is necessary for the subsequent free-field ground vibration calculations. Free boundary conditions are used at the ends of the track. There are 503 dofs for the rail and sleepers. In addition to this, the lumped parameter model for the half-space will introduce different numbers of dofs depending on the extent of the through-ground coupling. Lumped parameter models with $N_c = 0$ (i.e. no coupling), 1, 3 and 5 will introduce 404, 804, 1987 and 3414 additional dofs respectively into the FEM model. Even for the case of $N_c = 5$, these numbers are a small fraction of the dofs that would result from full time domain ground discretisation in the FEM.

### *7.1. Track and ground vibration*

Figure 7 shows the rail, sleeper and ground displacement magnitude and phase at the driving point for a unit harmonic load acting on the rail. The solutions obtained using the FEM with various extents of through-ground coupling, $N_c = 0$, 1, 3 and 5, are compared with the semi-analytical ones. Good agreement between the two methods can be observed, particularly for the rail and sleeper responses. For the case of $N_c = 0$, in which coupling in the ground occurs only through the rail, the rail and sleeper responses differ by at most 1 and 2 dB respectively but the ground response shows much larger discrepancies. There is no significant difference in the rail and sleeper responses obtained with $N_c = 1$, 3 or 5.

Resonances can be seen to occur at around 30-40 Hz and 200-210 Hz. In the first of these the whole track is bouncing on the ballast and ground stiffness, while in the second the rail is bouncing on the railpad stiffness. For the range of frequencies shown, the agreement in the ground displacement is also very good for $N_c = 1$, 3 or 5. This frequency range coincides with that for which ground vibration is significant.

Figure 8 shows the equivalent results for a point located at $x = 5\,\text{m}, y = 0$ (i.e. transfer receptances). For the case of $N_c = 0$ without through-ground coupling, the displacements are much lower at low frequencies where the ground response dominates, while the agreement is good for the rail and sleeper (but not for the ground) at higher frequencies. The necessity of having a wider extent of through-ground coupling is demonstrated in this example by the results obtained for $N_c = 5$ (which includes all cross-terms up to 3 m) being generally much closer to the semi-

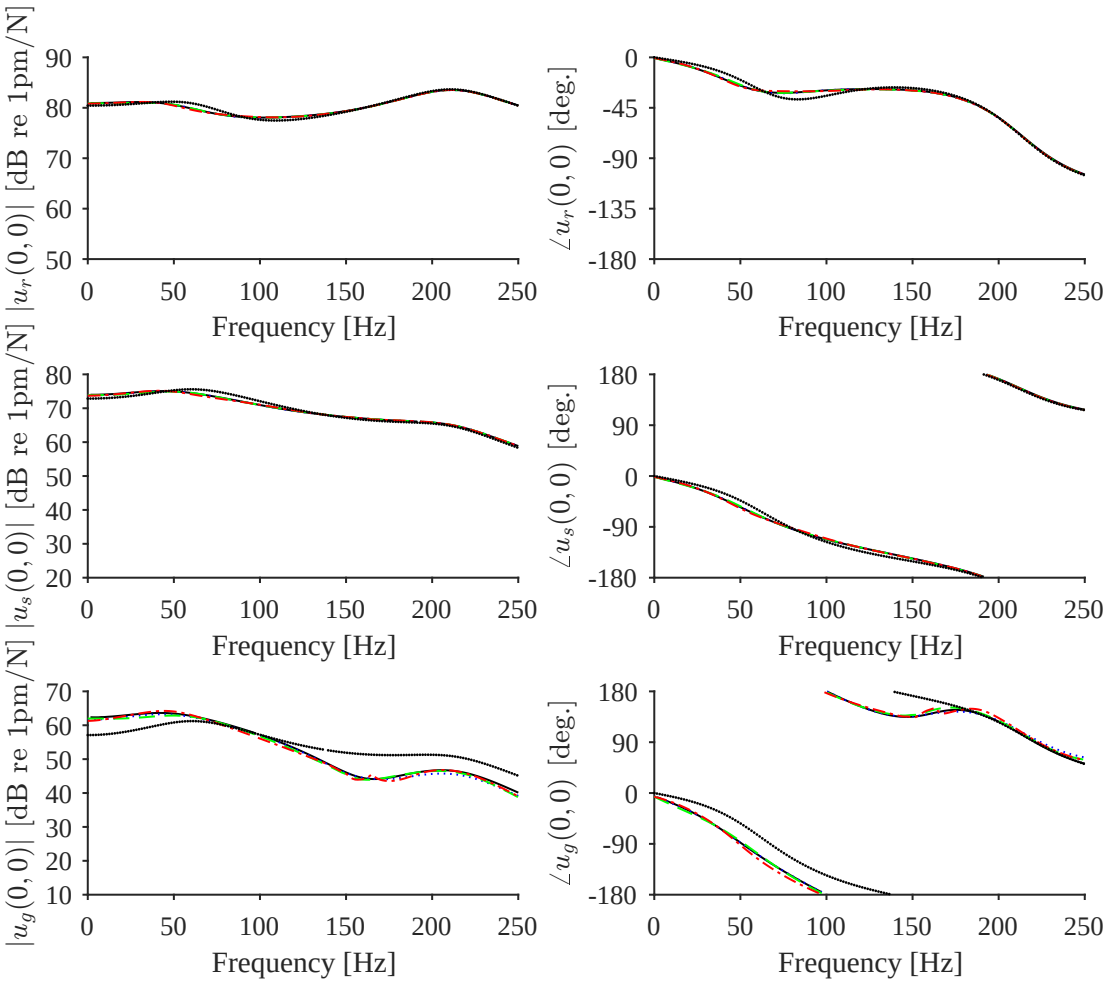


Figure 7: Receptance magnitude and phase of the rail (a-b), sleeper (c-d) and ground (e-f) under the driving point plotted against excitation frequency. Comparison between the semi-analytical model, (—) and the FEM with $N_c$ = 0, (. . .); 1, (· · · ); 3, (- - -) and 5, (-·-)

analytical solution.

It is clear, therefore, that the through-ground coupling is particularly important in modelling the transfer receptances. However, the peak displacements in this case are 14 dB, 17 dB and 10 dB lower than the corresponding driving point displacements of the rail, sleeper and ground respectively. Therefore it may be expected that the discrepancies here will have less effect on the far-field responses in the ground.

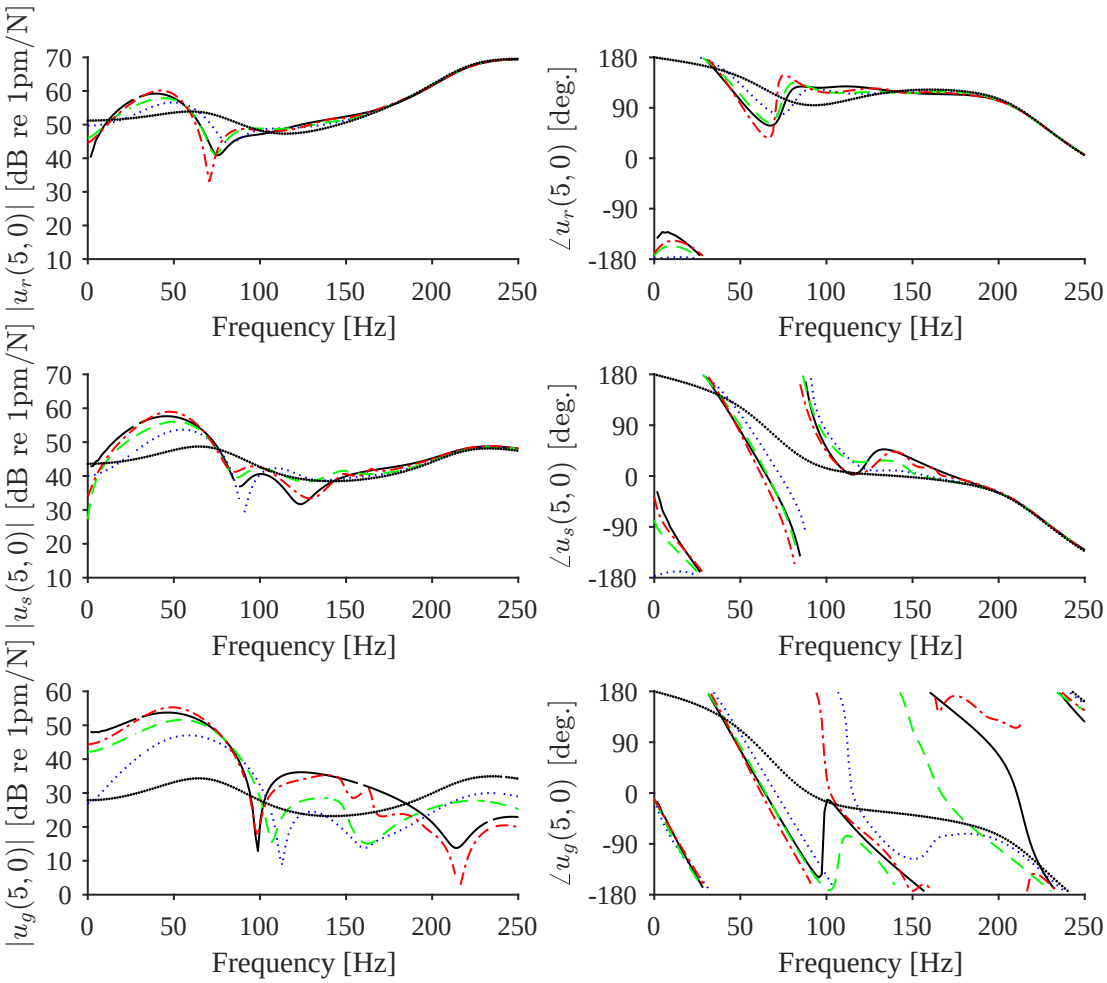


Figure 8: Transfer receptance magnitude and phase of the rail (a-b), sleeper (c-d) and ground (e-f) at $x = 5$ m, $y = 0$ plotted against excitation frequency. Comparison between the semi-analytical model, (—) and the FEM with $N_c = 0$, (. . .); 1, (· · ·); 3, (- - -) and 5, (-·-)

### *7.2. Interaction forces at the ballast/ground interface*

This section discusses the interaction forces at the ballast/ground interface. Figure 9(a,c) shows the amplitude of the force on the ground surface plotted against distance along the track due to a unit load on the rail that is oscillating at (a) 30 Hz and (c) 100 Hz. It shows a comparison between the semi-analytical model and the FEM with $N_c = 0$, 1, 3 and 5. In the FEM results, cubic spline curves are used to interpolate the results at discrete sleeper locations. In Fig. 9(a), all the results agree well in the vicinity of the load, up to about 3-4 sleeper bays ($\approx 1.8 - 2.4$ m), with

no significant improvement in accuracy for increasing values of $N_c$. Although the peak ground displacement predicted for $N_c = 0$ at 30 Hz is about 4.5 dB lower than the corresponding semi-analytical one (Fig, 5(e)), the interaction forces are quite similar. This can be attributed to higher effective stiffness of the ground when no through-ground coupling is considered. In Fig. 9(b), the case of $N_c = 0$ overestimates the peak force directly beneath the load by 1 dB whereas the other values of $N_c$ give better agreement with the semi-analytical solution. The influence of increasing

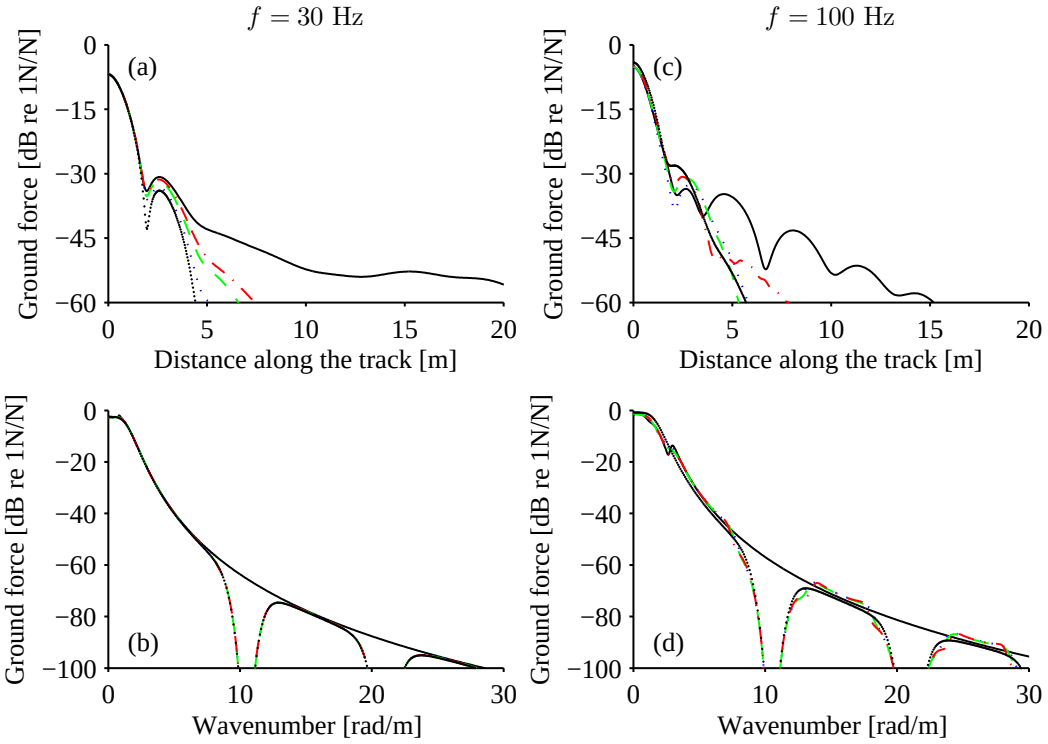


Figure 9: Ground force magnitude (a,c) in the space domain and (b,d) in the wavenumber domain, due to an oscillating load acting on the rail with frequency of (a,b) 30 Hz, (c,d) 100 Hz. Comparison between the semi-analytical model, (—) and the FEM with $N_c = 0$, (. . .); 1, (· · ·); 3, (- - -) and 5, (-·-))

$N_c$ is apparent in Fig. 9(a), however, for distances further away from the load. Notwithstanding this, the improvement occurs at regions with much lower force amplitudes, being less than 25 dB of the peak force, and their effects on the far field ground vibration are expected to be minimal.

As stated in Section 6, these forces need to be transformed to the wavenumber domain to be used as excitation for the ground model. Figure 9(b,d) shows the magnitude of the force on the

ground surface in the wavenumber domain for the same frequencies. In this case the effect of increasing $N_c$ in the FEM is not pronounced and they all agree well with the semi-analytical model away from regions where the dips occur. These dips are a direct consequence of the FEM being a discretely supported track model and occur at wavenumbers that are integer multiples of $2\pi/d$, i.e. 10.47 and 20.94 rad/m for the first two. However, the spectrum at these wavenumbers in the semi-analytical model is already 60 dB below the peak so the effect is expected to be small.

Figure 10 shows the magnitude and phase of the interaction force plotted against frequency for a load acting on the rail. The results are given for two positions; one located directly under the load

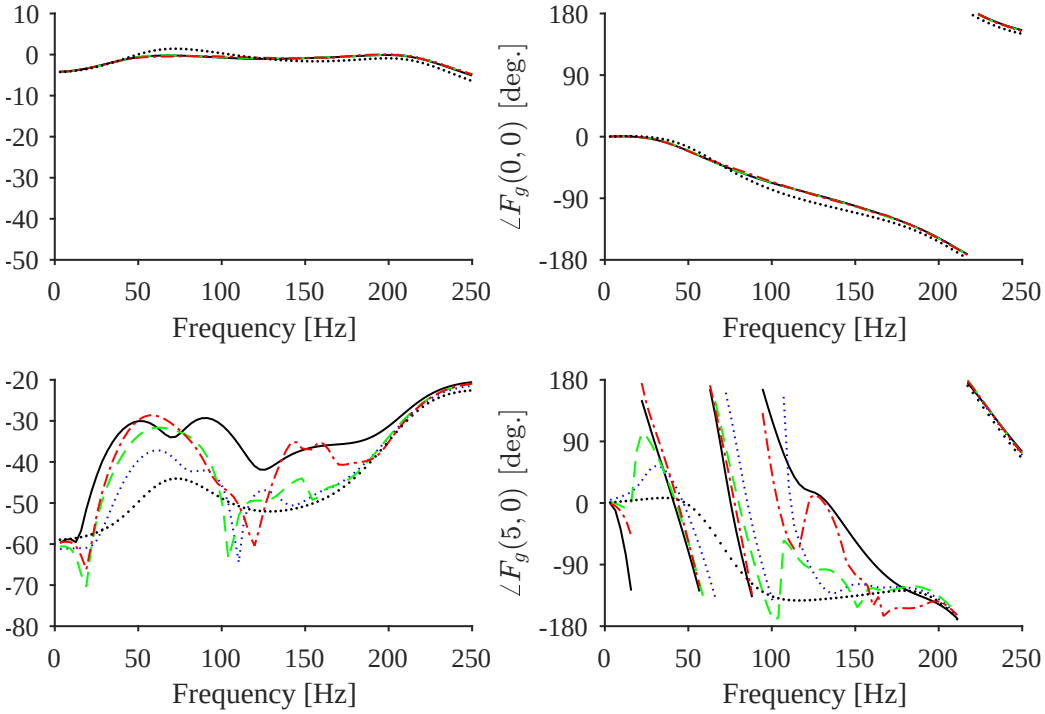


Figure 10: Magnitude and phase of the ground force at (a-b) $x = 0, y = 0$ and (c-d) $x = 5\text{m}, y = 0$ plotted against excitation frequency for a load acting on the rail. Comparison between the semi-analytical model, (—) and the FEM with $N_c = 0$, (. . .); 1, (· · ·); 3, (- - -) and 5, (-·-)

at $(x = 0, y = 0)$ and the other at $(x = 5\text{m}, y = 0)$. In Fig. 10(a-b), directly beneath the load, while the FEM results obtained for values of $N_c \geq 1$ closely match the semi-analytical solution, those for $N_c = 0$ deviate from it by as much as 1.5 dB. These differences are, however, much smaller than

those observed for the ground displacement in Fig. 5(e-f).

In Fig. 10(c-d), the predicted interaction force at the point away from the load indicates the benefit of a wider extent of through-ground coupling with increasing value of $N_c$. Again, since the peak force in this case is about 20 dB lower than those beneath the driving point, it is unlikely that it will significantly contribute to the dominant free-field ground vibration.

### *7.3. Free-field ground vibration spectra*

Using the calculated interaction forces at the ballast/ground interface as excitation for the ground model, free-field ground vibration can be calculated in accordance with the procedure described in Section 6.

In Fig. 11(a-b) the displacements of the ground surface are plotted as a function of distance away from the track along the line $x = 0$ for excitation frequencies of 30 Hz and 100 Hz respectively. These are calculated by applying the transformed forces (Fig. 9(b) and (d) respectively) to the half-space model in the wavenumber domain and performing the double inverse Fourier transformation to the space domain. Based on the good agreement for the interaction force at the regions of

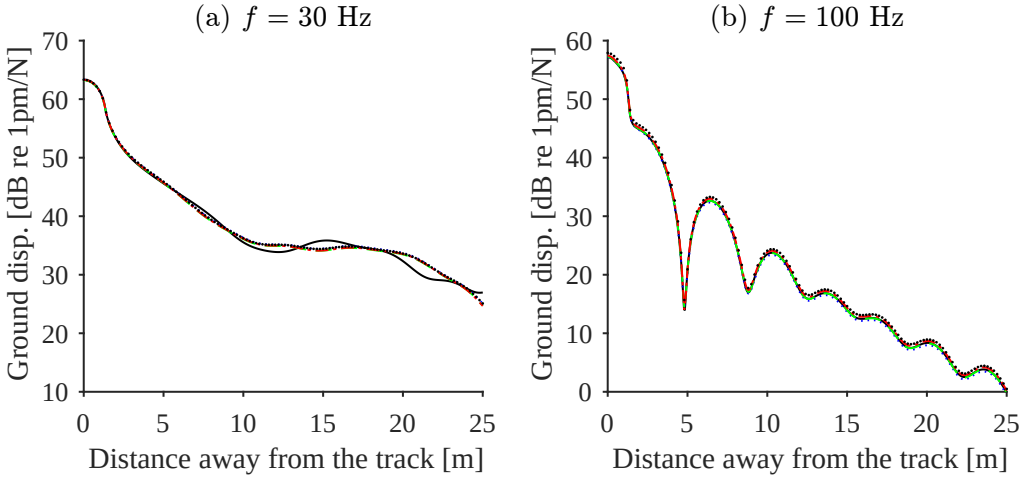


Figure 11: Displacement magnitude of the ground plotted against distance away from the track along the line $x = 0$ due for a load on the rail oscillating at (a) 30 Hz, (b) 100 Hz. Comparison between the semi-analytical model, (—) and the FEM with $N_c = 0$, (. . .); 1, (· · ·); 3, (- - -) and 5, (-·-)

larger amplitudes, it is confirmed that the ground vibration is very similar from both methods, par-

ticularly for the 100 Hz case. It has been demonstrated in Figs. 9 and 10 that the interaction forces at the ballast/ground interface predicted by the FEM have a better accuracy than the displacements used to calculate them, particularly in the vicinity of the load. When these forces are applied to the free-field ground model, the accuracy of the recalculated displacements is significantly enhanced. This is particularly true for the case of $N_c = 0$.

Figure 12 shows the magnitude and phase spectra of the displacements of the ground at three points located along the line $x = 0$ for $y = 0$, 8 and 16 m. The first case is for the driving point and has been presented in Fig. 5(e-f) as obtained directly in the FEM model. It is apparent that the results here for the FEM with $N_c = 0$ agree better with the semi-analytical solution. This is not surprising, since the discrepancies in the peak interaction forces are limited to 1.5 dB in the same frequency range. Similar agreement can be seen for the points in the far field, for which no significant differences are observed between the various values of $N_c$.

By comparing the ground displacements calculated in the first stage using the FEM, i.e. Fig. 5(e-f) and the free-field ones in Fig. 12, the importance of through-ground coupling in this case appears to be more significant for the prediction of the dynamic behaviour of the track than for the ground behaviour in the far field.

It is also of interest to investigate the ground response at points in the free field along $y$ for which $x$ does not coincide with the excitation point. Figure 13 shows the corresponding results for points located along the line $x = 5$ m for $y = 0$, 8 and 16 m. In this case, significant differences between the FEM and the semi-analytical solution are observed only for the point directly under the track (i.e. at $y = 0$). Different values of $N_c$ also lead to slightly different results. This is because the transfer receptances along the track (and hence interaction forces) are not predicted with the same accuracy as the point receptance (see Figs. 7, 8 and 10) and, although the magnitude of the force is lower in this region, it is large enough to affect the near-field response. However, the far-field responses in the case of $y = 8$ and 16 m are mainly affected by the larger force magnitudes in the vicinity of the load that are accurately predicted by the FEM, hence the good agreement. From these observations, it can be concluded that the case of $N_c = 0$ is good enough for the far-field vibration prediction, although a value of at least 1 would be required for track dynamics.

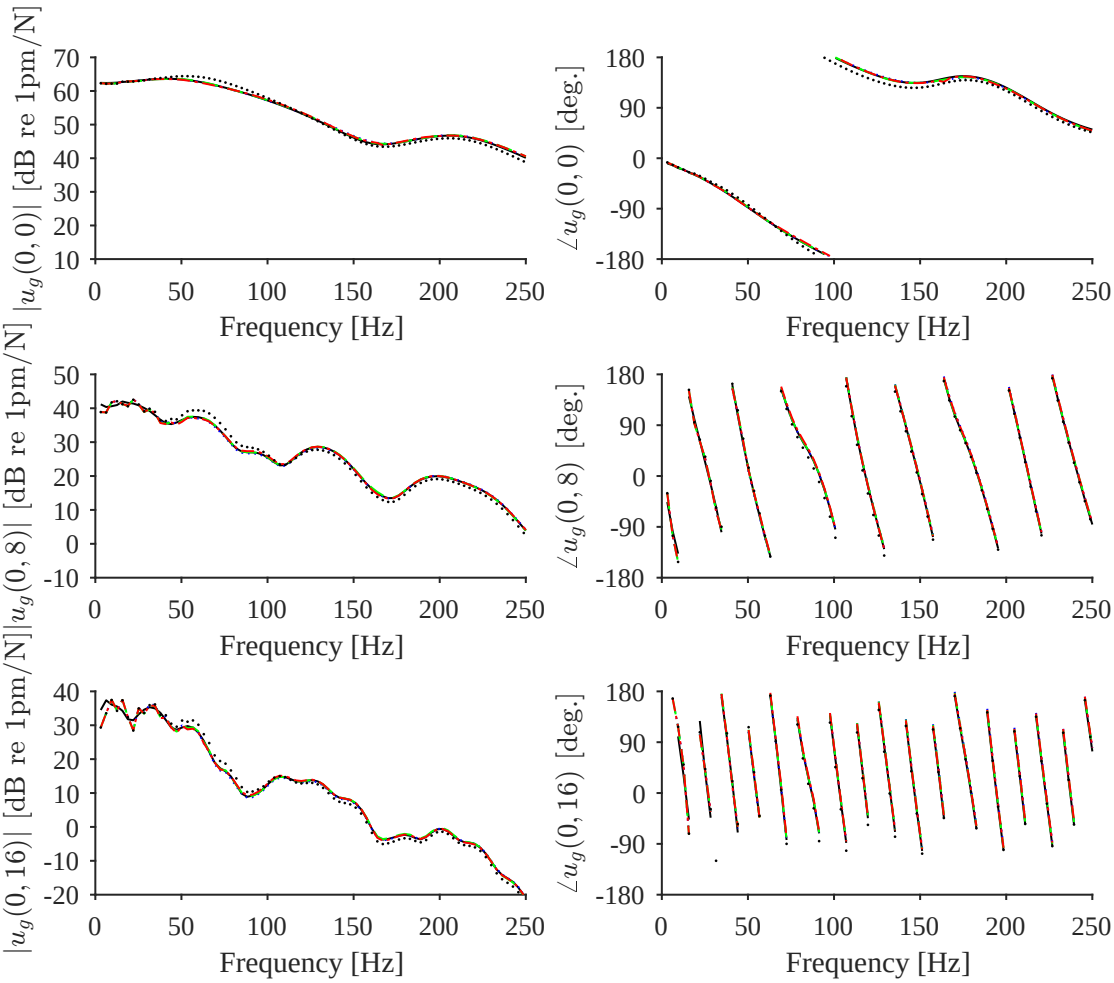


Figure 12: Magnitude and phase of the ground displacement at (a-b) $x = 0, y = 0$, (c-d) $x = 0, y =$ 8m and (e-f) $x = 0, y = 16$m, plotted against excitation frequency for a load acting on the rail. Comparison between the semi-analytical model, (—) and the FEM with $N_c = 0$, (. . .); 1, (· · ·); 3, (- - -) and 5, (-·-)

### *7.4. Effect of a layer overlying the half-space*

In order to demonstrate the applicability of the mixed formulation it is applied to a railway track resting on a layered ground. The dynamic stiffness in Eq. (9) is formulated using the Green's functions for a layered medium using the methodology of Kausel and Roësset [13]; alternatively it could be obtained by the flexibility formulations of Thomson [32] and Haskell [33]. Once the matrix is obtained, the process of forming the lumped parameter model and subsequent track/ground coupling, calculation of interaction force and free-field ground vibration remains unchanged.

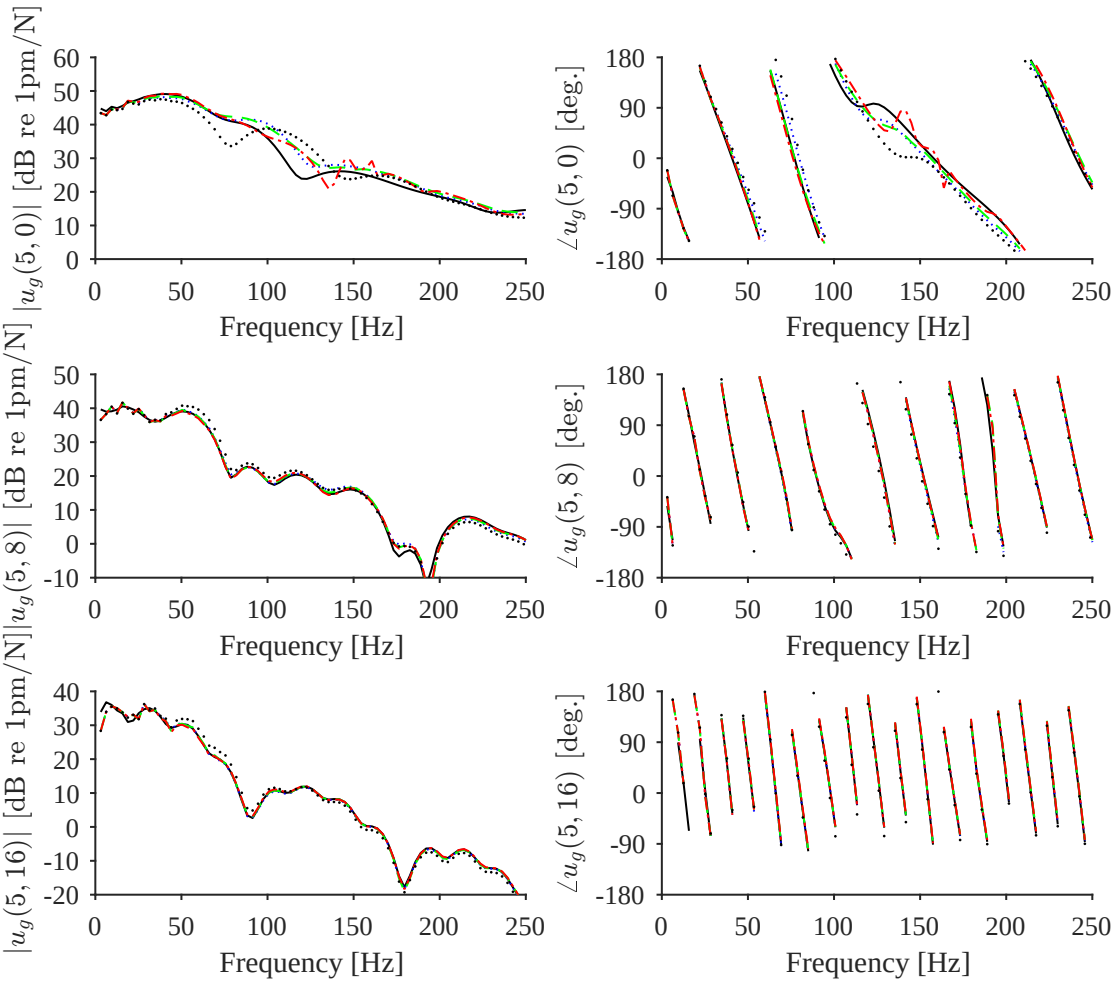


Figure 13: Magnitude and phase of the ground displacement at (a-b) $x = 5\text{m}, y = 0$, (c-d) $x = 5\text{m}, y = 8\text{m}$ and (e-f) $x = 5\text{m}, y = 16\text{m}$, plotted against excitation frequency for a load acting on the rail. Comparison between the semi-analytical model, (—) and the FEM with $N_c = 0$, (. . .); 1, (· · ·); 3, (- - -) and 5, (-·-)

The ground is considered to have a 3 m thick softer layer overlying the half-space. While the wave speeds of the half-space remain unchanged, those of the upper layer are $v_s = 175$ m/s and $v_p = 450$ m/s. The density and damping ratio are the same as for the half-space. In this case, the dimensionless frequency used in the curve fitting procedure for deriving the lumped parameter model is obtained using $v_s$ for the overlying layer. The lumped parameter models of the layered ground require more dofs than the half-space case. There are 804 dofs for the case of $N_c = 1$, 2085 for $N_c = 3$ and 3634 for $N_c = 5$. This should be expected as the dynamic behaviour of the layered

ground is more complex than the half-space.

The results obtained for the track receptances and interaction force at the ballast/ground interface show similarly good agreement with the semi-analytical solution as for the case of the half-space. However, only results for the free-field ground vibration are presented here.

Figure 14 shows the magnitude and phase spectra of the displacements of the ground at three points located along the line $x = 0$ for $y = 0$, 8 and 16 m. It compares the FEM solution with the semi-analytical one. It is apparent that both methods are in good agreement, with no significant differences between the various values of $N_c$ in the FEM results. Due to the relative softness of the overlying layer in comparison with the half-space, the magnitude of the ground displacement under the track is generally higher than for the case of the half-space (Fig. 12), with differences found of up to 8 dB. In the far-field cases, similar results are observed above 50 Hz, although the layered ground contains more fluctuating peaks and dips. These can be attributed to reflection and scattering of waves at the interface between the layer and the half-space. A peak, centred at about 25 Hz exists in all cases, with the peak displacement magnitude at $y = 8$ and 16 m respectively being 7.1 dB and 7.5 dB higher than the corresponding peak displacements for the half-space case.

Finally, Fig. 15 shows the corresponding results for points located along the line $x = 5$ m for $y = 0$, 8 and 16 m. As with the half-space case (Fig. 13), some discrepancies exist between the semi-analytical and FEM solutions for the point under the track. Moreover, some differences also exist within the FEM results for the various $N_c$ values. The same explanation given for the half-space case also applies here. However, as a direct consequence of the accurate predictions of the interaction force in the vicinity of the load- where its magnitude is greatest- the far field responses at $y = 8$ and 16 m are accurately predicted for all values of $N_c$.

## 8. Case study: time domain analysis

In this section, the lumped parameter model of the ground will be demonstrated in a transient time domain analysis. Results are only presented for the homogeneous half-space model of the ground. Similar to the frequency domain analysis, a stationary load will be applied on the rail and the displacements of the rail, sleeper and ground will be computed together with the interaction

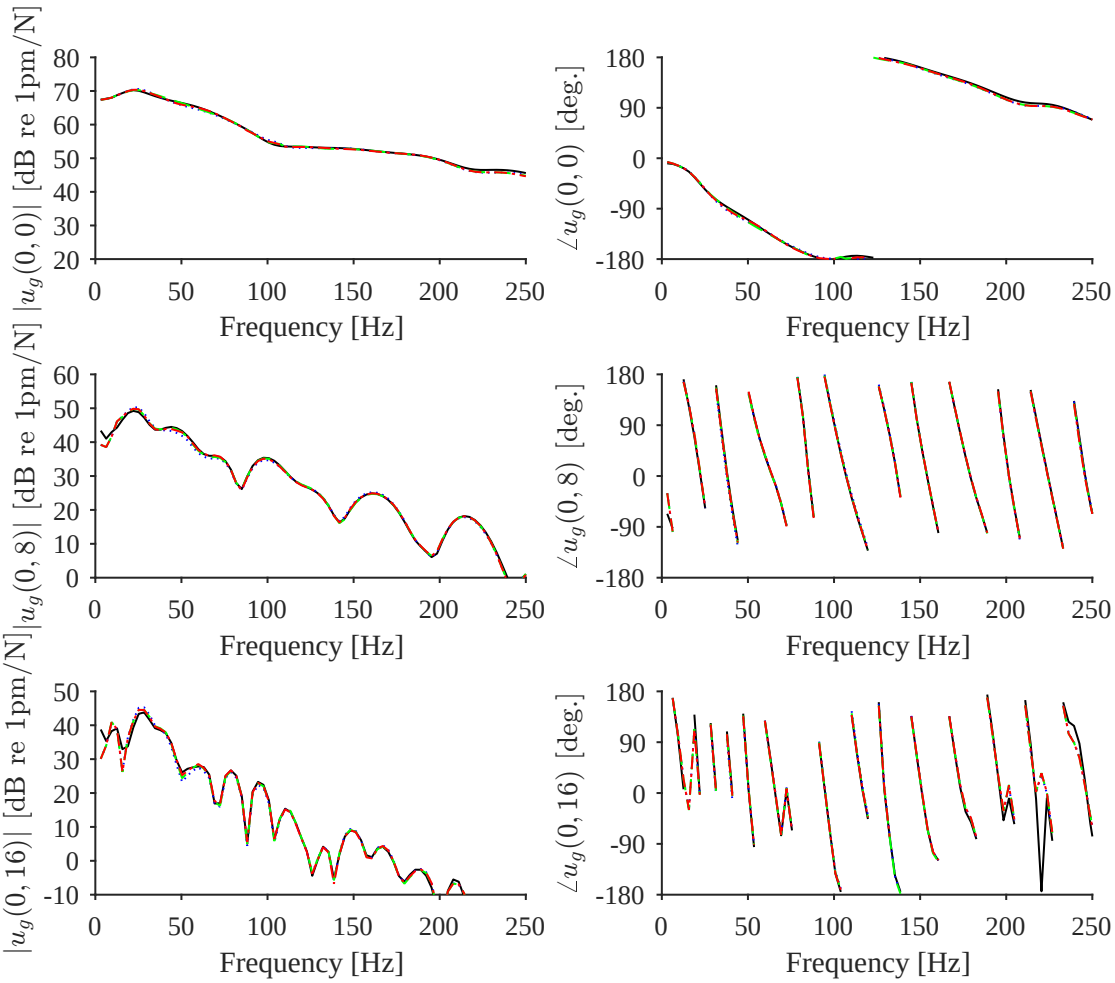


Figure 14: Magnitude and phase of the layered ground displacement at (a-b) $x = 0, y = 0$, (c-d) $x = 0, y = 8$m and (e-f) $x = 0, y = 16$m, plotted against excitation frequency for a load acting on the rail. Comparison between the semi-analytical model, (—) and the FEM with $N_c = 1$, (· · ·); 3, (- - -) and 5, (-·-)

force at the ballast/ground interface. However, the load is defined here as a Ricker wavelet, which is a good example of a signal that contains a spectrum of frequencies. This is expressed as [34]

$$p(t) = \left[1 - 2\left(\pi f_p(t - t_0)\right)^2\right] \mathrm{e}^{-\left(\pi f_p(t-t_0)\right)^2} \tag{34}$$

where $f_p$, termed the peak frequency, is the frequency with the largest spectral amplitude, $t$ is time and $t_0$ is the time delay at which the peak in the wavelet occurs.

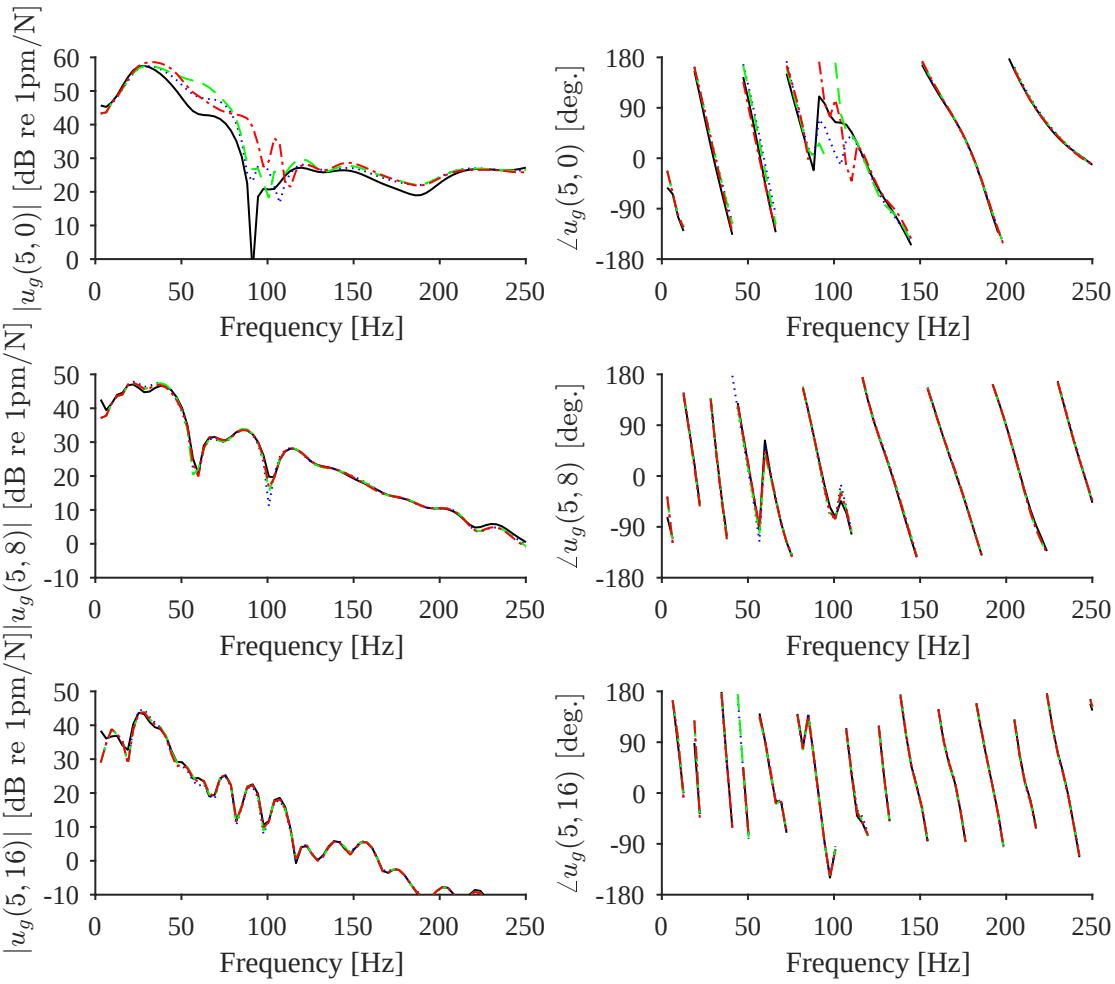


Figure 15: Magnitude and phase of the layered ground displacement at (a-b) $x = 5\text{m}, y = 0$, (c-d) $x = 5\text{m}, y = 8\text{m}$ and (e-f) $x = 5\text{m}, y = 16\text{m}$, plotted against excitation frequency for a load acting on the rail. Comparison between the semi-analytical model, (—) and the FEM with $N_c = 1$, (· · ·); 3, (- - -) and 5, (-·-)

The Fourier transform of Eq. (34) is given as

$$\hat{P}(\omega) = \frac{2}{\sqrt{\pi} f_p} \left( \frac{\omega}{2\pi f_p} \right)^2 \mathrm{e}^{-\left(\mathrm{i}\omega t_0 + (\omega/2\pi f_p)^2\right)}. \tag{35}$$

The effect of the delay is a shift in the phase but not a change in the amplitude.

Figure 16 shows the magnitude spectrum of a Ricker wavelet with $f_p = 50$ Hz and $t_0 = 0$. Also shown is the wavelet as a time series. The spectrum can be seen to contain significant spectral

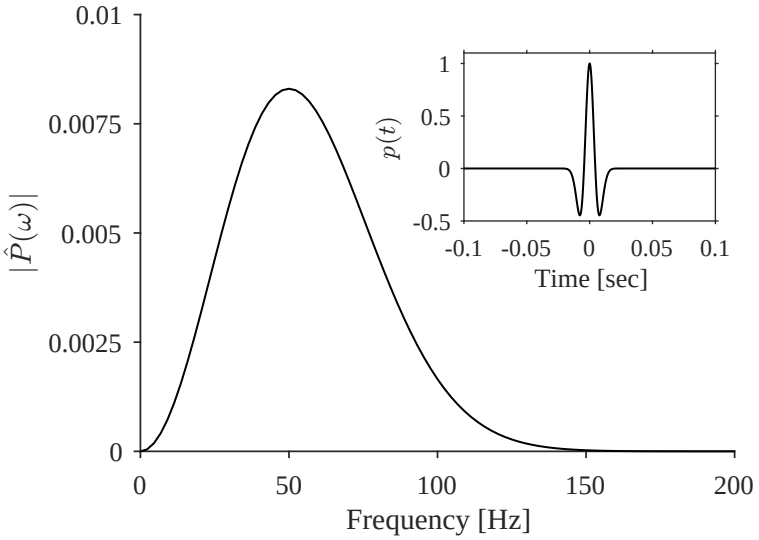


Figure 16: Magnitude spectrum of a Ricker wavelet (time signal shown in plot) with $f_p = 50$ Hz and $t_0 = 0$ seconds

content in a wide band of frequencies up to $3f_p$.

*8.1. Time domain results for linear track parameters*

In this section, linear track parameters will be used to compare the results of the FEM with those of the semi-analytical model.

In the time domain model the time series of the Ricker wavelet is applied directly as the excitation force. The displacements of the track, including the ground nodes under the track, are obtained using a two sub-step time integration scheme [31]. The time step of $dt = T_p/20$ was used in the computations, where $T_p = 1/f_p$, and the total simulation time was chosen as an integer multiple of $T_p$.

The calculations are also performed in the wavenumber-frequency domain for comparison. This is done as follows. The Fourier transform of the time series of the wavelet is obtained. For each discrete frequency of the spectrum, $\omega_j$, a harmonic load of frequency $\omega_j$ and amplitude corresponding to the amplitude of the spectrum at $\omega_j$, is applied on the rail. The problem is solved in the wavenumber-frequency domain and the responses of the track and ground are converted to the space-time domain using the inverse Fourier transform. The total response is a superposition

of the individual space-time domain responses as follows

$$U(x,t) = \sum_{j=1}^{N_\omega} u_j(x,t)\cos(\omega_j t), \tag{36}$$

where $u_j(x,t)$ is the response for each excitation frequency, and $N_\omega$ is the number of frequencies included in the spectrum. Because of the shape of the frequency spectrum, it is possible to truncate frequencies with sufficiently small amplitudes without compromising the accuracy of the solution. For example, although the sampling frequency for a wavelet with very small time step will be large, significant spectral content is only found at frequencies up to $3f_p$.

Figure 17 shows a comparison of the results obtained with the time-domain FE model and wavenumber-frequency domain model for $f_p = 50$ Hz. The left-hand plots contain the displacements of the rail, sleeper and ground respectively underneath the driving point (i.e. $x = 0, y = 0$), and the interaction force at the ballast ground interface at the same point. The corresponding results for a point located at ($x = 3, y = 0$) are shown in the right-hand plots. At the loading point the results from the two models are almost indistinguishable. At this frequency the shape of the response is similar to that of the excitation, although propagating waves have started to form. Some small differences are found between the two models for the results at 3 m away, but with $N_c = 3$ in the FEM, these differences can be expected.

### *8.2. Consideration of nonlinear track parameters*

In this section the analysis will be extended to include nonlinear track parameters in the FEM to demonstrate its ability to deal with such problems. New stiffness values are defined for the railpads and ballast in order to represent their behaviour, while the other parameters in Table 2 remain unchanged. The nonlinear static load-deflection relationship of a studded rubber type railpad was measured in the laboratory, whereas data reported in [35] have been used for the ballast. Using the *fminsearch* curve fitting routine in MATLAB, optimal polynomials were fitted to the railpad and ballast data to represent the relationship between the applied forces and corresponding

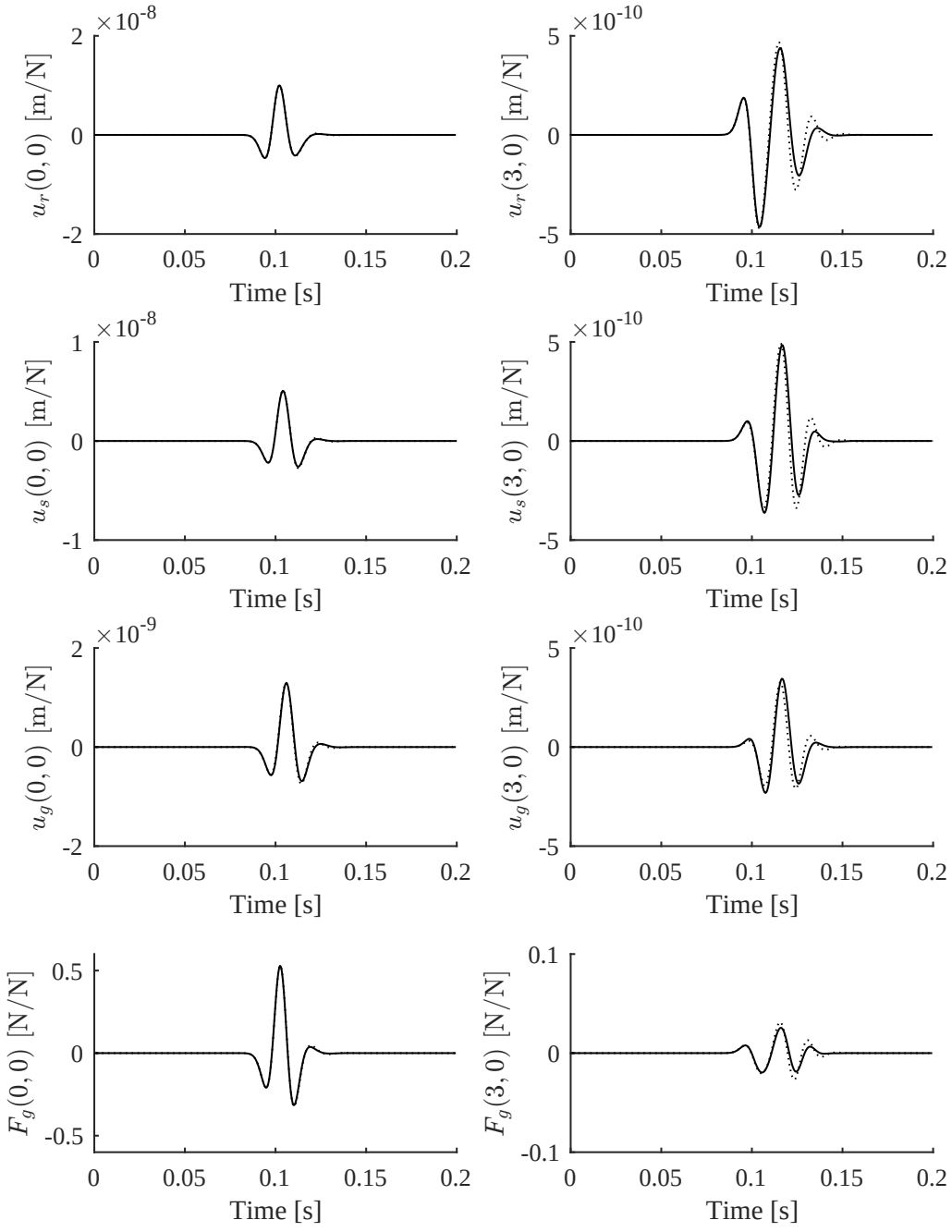


Figure 17: Rail, sleeper and ground displacements and interaction forces at the ballast/ground interface due to a Ricker pulse with $f_p$ = 50 Hz. Comparison between the semi-analytical model (—), and the FEM with $N_c$ = 3 ($\cdots$)

displacements. These are given respectively for the railpad and ballast as

$$F_p(u_p) = 38.82u_p + 157.10 \times 10^6 u_p^3 \quad \text{MN} \tag{37}$$

and

$$F_b(u_b) = 49.71u_b - 16.58 \times 10^7 u_b^3 + 50.44 \times 10^{14} u_b^5 \quad \text{MN}, \tag{38}$$

where $u_p$ and $u_b$ are the displacements (in metres) of the railpad and ballast respectively and $F_p$ and $F_b$ the corresponding forces (in Newtons). Additionally, two rails are included in the model.

In railway track dynamics, the load can be divided into two components; the static load component resulting from the weight of the train, and the dynamic wheel-rail interaction forces. Here the former will be treated as a stationary static preload applied on the track. The resulting static displacements of the railpads and ballast are nonlinear functions of the loads acting at the sleeper positions. However, since the dynamic displacements are small, it is assumed that they are in linear relation with the dynamic loading. The dynamic loading, superimposed on the static preload, can be described as being harmonic, random or any time varying function.

For the static part of the analysis, the system of nonlinear equations, $\left[\mathbf{K}^{t/g}(\mathbf{U}^{t/g})\right]\left\{\mathbf{U}^{t/g}\right\} = \left\{\mathbf{F}^{t/g}\right\}$, is solved iteratively [31] using the Newton-Raphson iterative routine to obtain the equilibrium state of the track/ground system (i.e. the global displacements) due to the static load, and hence the nonlinear stiffness values of the railpads and ballast at state.

Figure 18 shows the variation of the tangent static stiffness of the railpads and ballast due to the application of a static load of 70 kN on each rail. It can be seen that the static preload induces a nonlinear stiffness profile of the railpad and ballast. Consequently, the railpads and ballast closest to the position of the load become considerably stiffer than those further away which remain unloaded. For the railpad, there is a factor of about 3.3 between the maximum and unloaded stiffness values, whereas a much higher factor of 12 factor is found for the ballast.

Using these nonlinear stiffness values of the railpads and ballast, the dynamic behaviour of the track/ground system can be studied by applying any form of time varying loading. Note that the static load is not included in this part of the analysis, since its effect is already accounted for in the

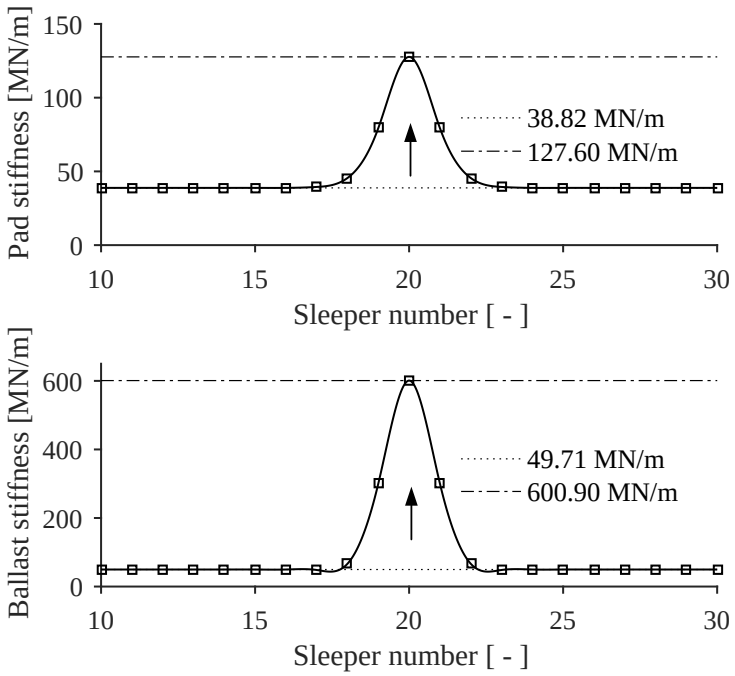


Figure 18: Loaded stiffness (tangent) distribution of the railpads and ballast induced by a static load on each rail. Also showing the unloaded and maximum loaded stiffness values. □: stiffness at sleeper positions, —: interpolated stiffness.

nonlinear stiffness profiles [36]. For comparison, the unloaded stiffness values will be used for the linear model. A more rigorous way of choosing an equivalent linear stiffness can be devised, but this is not pursued here.

It should be noted that the nonlinear analysis need not be limited to the static part of the load. In principle, nonlinear dynamic analysis can also be considered in the model but this requires better characterisation of the dynamic stiffness of railpads and ballast. Such characterisation is being developed by the current authors.

Figure 19 shows the maximum displacements of the rail, sleeper and ground, at the driving point and at 3 m away from the driving point along the $x-$direction. Also plotted are the interaction forces at the ballast/ground interface. These were calculated by applying a unit harmonic load in the form $\cos \omega t$ on each rail for a duration corresponding to 20 cycles. Transient dynamic effects are minimised by applying a 20% Tukey window to the loading. For each frequency, the solution is obtained by time integration and the maximum displacement and force amplitudes were recorded.

The disparities between the two models are clearly visible, not only in the amplitudes but also

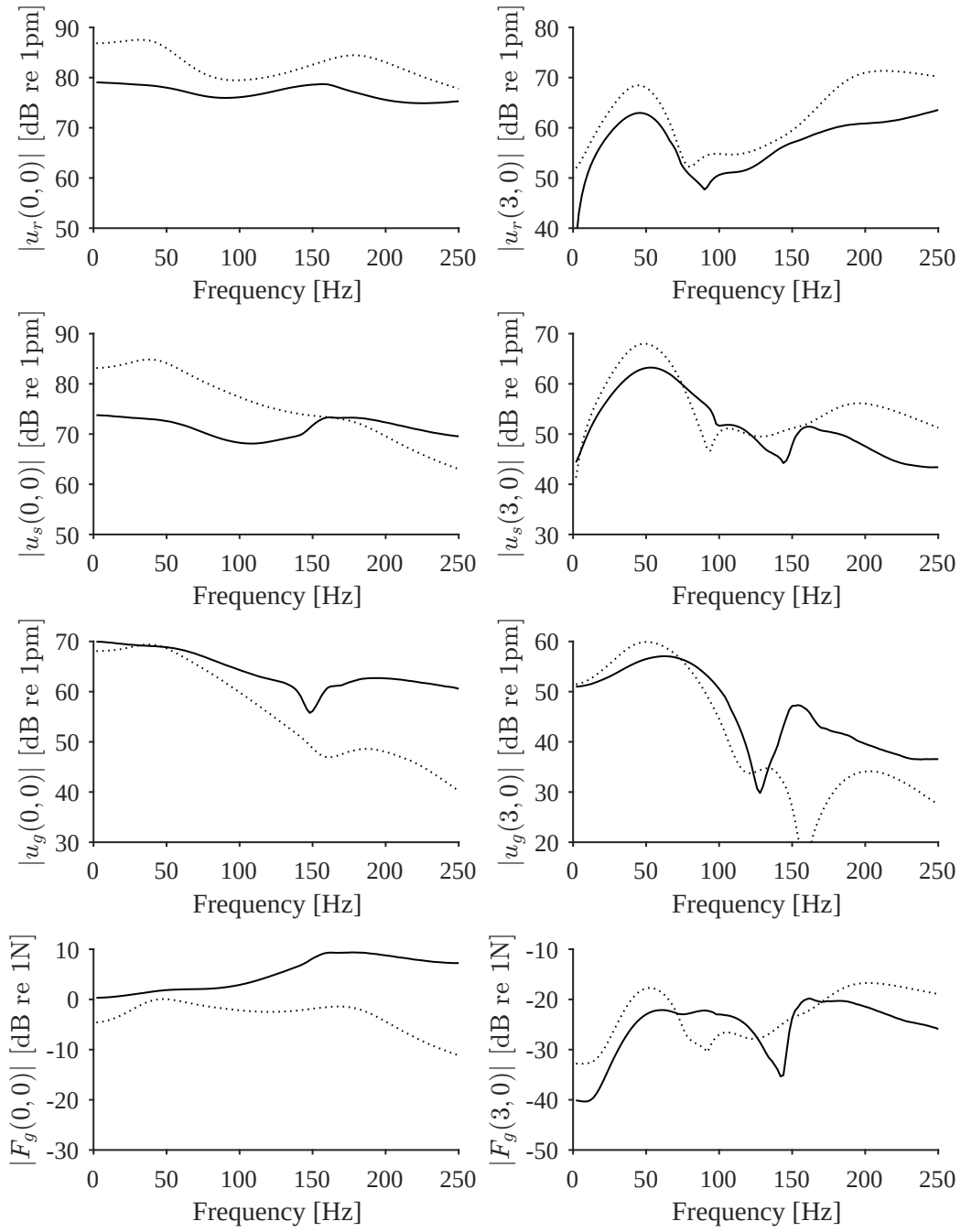


Figure 19: Displacement spectra of the rail, sleeper and ground under the driving point and at 3 m away from the driving point. The spectra of the force at the ballast/ground interface at these points are also shown. Comparison between the linear (**. . .**) and nonlinear (**—**) models

in the frequencies at which the peaks occur. Generally, it is expected that the loaded stiffness of the railpads and ballast will result in lower displacements for the rail and sleepers. However, this also results in increased forces transmitted through these components, so that at the ballast/ground contact, the force levels are considerably higher for the nonlinear case. The implications for this are higher levels of ground vibration both under the driving point and at distances away.

For the sake of brevity, further results have not been shown for the free-field ground vibration. The process of transforming the interaction forces at the ballast/ground interface from the space domain to the wavenumber domain remains unchanged. Due to the transient nature of the load, however, a Fourier transformation from time to frequency domain is also necessary. Subsequently, the method of calculating the free-field ground vibration at any frequency that is represented in the spectra of the interaction force remains unchanged.

## 9. Conclusions

A systematic procedure has been presented that utilises both space-time and wavenumber-frequency domain modelling techniques to predict ground vibration from a surface railway track. The railway track is modelled in the space-time domain using the Finite Element (FE) method, whereas the ground is modelled in the wavenumber-frequency domain. The vertical dynamic stiffness matrix is derived for the interaction of a series of rectangular strips located at the surface of the ground that are used to couple the track to the ground. To include the ground into the FE track model, the elements of the dynamic stiffness matrix are represented by discrete lumped parameter models. The interaction between strips is modelled to varying extent, since through-ground coupling between strips is expected to extend only to a finite region along the track. Firstly, frequency domain analysis is conducted by applying a stationary harmonic load on the rail, and directly calculating the steady-state solutions. The interaction force at the ballast/ground interface is calculated in the space-time domain, transformed to the wavenumber domain, and used as input to the ground model for calculating vibration in the far field. Time domain analysis is also performed for both linear and nonlinear track parameters to demonstrate the operation of the mixed formulation.

This approach is applied to a railway track resting on a ground that is modelled firstly as a half-space and then as a layer overlying a half-space. For both set of analyses and for linear parameters,

the current model gives accurate predictions of the dynamic response of track/ground system and the interaction force at the track/ground interface, in comparison with a semi-analytical model formulated in the wavenumber-frequency domain. This is particularly true for the vicinity of the excitation point. The response at other points along the track that are further away from the excitation point can be modelled more accurately by increasing the extent of through-ground coupling. Through-ground coupling has been found to be necessary for both track dynamics and ground vibration predictions. Comparison of the far-field ground vibration also shows good agreement for both the half-space and layered half-space cases.

Being an approximate method for solving the linear or nonlinear railway track-ground interaction problem with considerably smaller system matrices, this approach serves as an attractive alternative to full space-time domain discretisation using Finite Element and/or Boundary Element methods. Since the lumped parameter model of the ground is formulated with frequency-independent spring, dashpot and mass components, extension to the case of a moving load- which would give rise to multiple receiving frequencies in both the track and ground- is also possible.

## Acknowledgements

This work is undertaken as part of the MOTIV (Modelling of Train Induced Vibration) project which is funded by the EPSRC under grants EP/K005847/2 and EP/K006002/1.

## References

[1] X. Sheng, C.J.C. Jones, and M. Petyt. Ground vibration generated by a harmonic load acting along a railway track. *Journal of Sound and Vibration*, 225(1):3–28, 1999.

[2] X. Sheng, C.J.C. Jones, and M. Petyt. Ground vibration generated by a load moving along a railway track. *Journal of Sound and Vibration*, 228(1):129–156, 1999.

[3] X. Sheng, C.J.C. Jones, and D.J. Thompson. A comparison of a theoretical model for quasi-staically and dynamically induced environmental vibration from trains with measurements. *Journal of Sound and Vibration*, 267:621–635, 2003.

[4] X. Sheng, C.J.C. Jones, and D.J. Thompson. Prediction of ground vibration from trains using the wavenumber finite and boundary element methods. *Journal of Sound and Vibration*, 293: 575–586, 2006.

[5] P. Galvín, S. François, M. Schevenels, E. Bongini, G. Degrande, and G. Lombaert. A 2.5d coupled fe-be model for the prediction of railway induced vibrations. *Soil Dynamics and Earthquake Engineering*, 30(12):1500–1512, 2010.

[6] G.Y. Gao, Q.S. Chen, J.F. He, and F. Liu. Investigation of ground vibration due to trains moving on saturated multi-layered ground by 2.5d finite element method. *Soil Dynamics and Earthquake Engineering*, 40:87 – 98, 2012.

[7] P. Galvín, A. Romero, and J. Domínguez. Fully three-dimensional analysis of high-speed traintracksoil-structure dynamic interaction. *Journal of Sound and Vibration*, 329(24):5147 – 5163, 2010.

[8] P.A. Costa, R. Calçada, A.S. Cardoso, and A. Bodare. Influence of soil non-linearity on the dynamic response of high-speed railway tracks. *Soil Dynamics and Earthquake Engineering*, 30(4):221 – 235, 2010.

[9] George Gazetas. Analysis of machine foundation vibrations: State of the art. *International Journal of Soil Dynamics and Earthquake Engineering*, 2(1):2 – 42, 1983.

[10] G. Kouroussis, G. Gazetas, I. Anastasopoulos, C. Conti, and O. Verlinden. Discrete modelling of vertical track-soil coupling for vehicle-track dynamics. *Soil Dynamics and Earthquake Engineering*, 31(12):1711–1723, 2011.

[11] G Kouroussis, O Verlinden, and C Conti. A two-step time simulation of ground vibrations induced by the railway traffic. *Proceedings of the Institution of Mechanical Engineers, Part C: Journal of Mechanical Engineering Science*, 226(2):454–472, 2012.

[12] N. Triepaischajonsak and D.J. Thompson. A hybrid modelling approach for predicting ground vibration from trains. *Journal of Sound and Vibration*, 335:147–173, 2015.

[13] E. Kausel and J.M. Roësset. Stiffness matrices for layered soils. *Bulletin of the Seismological Society of America*, 71(6):1743–1761, 1981.

[14] J.C.O. Nielsen, G. Lombaert, and S. François. A hybrid model for prediction of ground-borne vibration due to discrete wheel/rail irregularities. *Journal of Sound and Vibration*, 345:103 – 120, 2015.

[15] J.C.O. Nielsen and A. Igeland. Vertical dynamic interaction between train and track influence of wheel and track imperfections. *Journal of Sound and Vibration*, 187(5):825–839, 1995.

[16] G. Lombaert, G. Degrande, J. Kogut, and S. François. The experimental validation of a numerical model for the prediction of railway induced vibrations. *Journal of Sound and Vibration*, 297(3-5):512–535, 2006.

[17] J.P. Wolf. Consistent lumped-parameter models for unbounded soil: Physical representation. *Earthquake Engineering & Structural Dynamics*, 20(1):11–32, 1991.

[18] J. P. Wolf. Consistent lumped-parameter models for unbounded soil: Frequency-independent stiffness, damping and mass matrices. *Earthquake Engineering & Structural Dynamics*, 20 (1):33–41, 1991.

[19] M. Damgaard, L.V. Andersen, and L.B. Ibsen. Computationally efficient modelling of dynamic soil-structure interaction of offshore wind turbines on gravity footings. *Renewable Energy*, 68(0):289 – 303, 2014.

[20] M. Damgaard, V. Zania, L.V Andersen, and L.B. Ibsen. Effects of soil-structure interaction on real time dynamic response of offshore wind turbines on monopiles. *Engineering Structures*, 75(0):388 – 401, 2014.

[21] D.V. Jones, D. Le Houedec, and M. Petyt. Ground vibrations due to a rectangular harmonic load. *Journal of Sound and Vibration*, 212(1):61–74, 1998.

[22] L. Andersen and J. Clausen. Impedance of surface footings on layered ground. *Computers & Structures*, 86(1-2):72–87, 2008.

[23] K.F. Graff. *Wave Motion in Elastic Solids*. Dover publications, inc., New York, 1991.

[24] S.G. Koroma, D.J. Thompson, M.F.M. Hussein, and E. Ntotsios. A mixed space-time and wavenumber domain model for predicting ground vibration from railway tracks. In *COMPDYN 2015: Computational Methods in Structural Dynamics and Earthquake Engineering, Crete, Greece*, pages 96–106, 2015.

[25] L. Andersen. Assessment of lumped-parameter models for rigid footings. *Computers & Structures*, 88(23-24):1333–1347, 2010. Special Issue: Association of Computational Mechanics United Kingdom.

[26] L.B. Ibsen and M. Liingaard. Lumped-parameter models. DCE Technical Report No. 11, Aalborg University, 2006.

[27] L.B. Ibsen and M. Liingaard. Application of lumped-parameter models. DCE Technical Report No. 12, Aalborg University, 2006.

[28] L. Andersen and M.A. Liingaard. Lumped-parameter models for wind-turbine footings on layered ground. In B.H.V. Topping, editor, *Proceedings of the Eleventh International Conference on Civil, Structural and Environmental Engineering Computing*, number 227. Civil-Comp Press, Stirlingshire, UK,, 2007.

[29] M.A. Dokainish and K. Subbaraj. A survey of direct time-integration methods in computational structural dynamics-i. explicit methods. *Computers & Structures*, 32(6):1371 – 1386, 1989.

[30] K. Subbaraj and M.A. Dokainish. A survey of direct time-integration methods in computational structural dynamics-ii. implicit methods. *Computers & Structures*, 32(6):1387 – 1401, 1989.

[31] K-J Bathe and M.M.I. Baig. On a composite implicit time integration procedure for nonlinear dynamics. *Computers & Structures*, 83:2513–2524, 2005.

[32] W.T. Thomson. Transmission of elastic waves through a stratified solid medium. *Journal of Applied Physics*, 21(2):89–93, 1950.

[33] N. A. Haskell. The dispersion of surface waves on multilayered media. *Bulletin of the Seismological Society of America*, 43(1):17–34, 1953.

[34] J.B. Schneider. Understanding the finite-difference time-domain method. 2010. URL `www.eecs.wsu.edu/~schneidj/ufdtd`.

[35] J.C.O. Nielsen and J. Oscarsson. Simulation of dynamic train-track interaction with state-dependent track properties. *Journal of Sound and Vibration*, 275:515–532, 2004.

[36] S.G. Koroma, M.F.M. Hussein, and J.S. Owen. Influence of preload and nonlinearity of railpads on vibration of railway tracks under stationary and moving harmonic loads. *Low Frequency Noise, Vibration and Active Control*, 34(3):289–306, 2015.